NASA TECHNICAL NOTE

$C.1$

AN AERODYNAMIC ANALYSIS
OF SATURN I BLOCK I
FLIGHT TEST VEHICLES

by Fernando S. Garcia

George C. Marshall Space Flight Center
Huntsville, Alabama

NATIONAL AERONAUTICS AND SPACE ADMINISTRATION • WASHINGTON, D. C. • FEBRUARY 1964

AN AERODYNAMIC ANALYSIS OF SATURN I BLOCK I FLIGHT

TEST VEHICLES

By Fernando S. Garcia

George C. Marshall Space Flight Center
Huntsville, Alabama

NATIONAL AERONAUTICS AND SPACE ADMINISTRATION

TABLE OF CONTENTS

LIST OF ILLUSTRATIONS

LIST OF ILLUSTRATIONS (CONCL'D)

DEFINITION OF SYMBOLS

Symbol	Definition
a_L	Longitudinal acceleration
C_{D_b}	Base drag coefficient
C_{m_α}	Gradient of moment coefficient about center of gravity per unit angle-of-attack
C_p	Pressure coefficient, $\dfrac{P - P_a}{q}$ or $\dfrac{P/P_a - 1}{(\gamma/2) M^2}$
$\Delta C_{P(rms)}$	Coefficient of root-mean-square pressure fluctuations about the mean, $\overline{P}/q$
C_x	Axial force coefficient
C_z'	Gradient of normal force coefficient per unit angle-of-attack
CG	Distance of center of gravity from gimbal plane
CP	Distance of center of pressure from gimbal plane
D	Reference diameter (6.528 m)
D_t	Aerodynamic and fuel flow damping constant
F	Total axial thrust
F'	Engine thrust corrected for cant angle
I	Vehicle mass moment of inertia
M	Free-stream Mach number
m	Total vehicle mass
p	Static pressure
$\overline{P}$	Root-mean-square value of pressure fluctuations

DEFINITION OF SYMBOLS (Concl'd)

Symbol	Definition
$\overline{P}_r$	Reference sound level pressure
q	Free-stream dynamic pressure
S	Reference area (33.47 m^2)
SPL	Sound pressure level in decibels
S_B	Total base area
S_{B_N}	Total nozzle exit area
α	Free-stream angle-of-attack
β	Outboard engine deflection
γ	Ratio of specific heats for air (1.4)
$\ddot{\gamma}$	Normal acceleration
$\dot{\varphi}$	Angular velocity
$\ddot{\varphi}$	Angular acceleration

Subscript	Definition
$1, 2 \ldots$	Indicate engine number
a	Ambient conditions
b	Base
s	Local surface conditions
o	Outboard engine
p	Pitch plane
y	Yaw plane

AN AERODYNAMIC ANALYSIS OF SATURN I BLOCK I FLIGHT
TEST VEHICLES

By Fernando S. Garcia

SUMMARY

This report presents a summary of results from the aerodynamic flight evaluation of Saturn I, Block I vehicles (SA-1 through SA-4). The evaluation of telemetered data included axial force calculations, stability analysis, and environmental steady-state and fluctuating pressure data analyses. Comparisons are made with wind tunnel and/or theoretical, predicted values.

The axial force coefficient, obtained as a by-product of engine performance evaluation, was nearly identical for SA-1 and SA-2 with values falling roughly 15 per cent less than predicted for Mach numbers above 0.7. SA-4 values, as expected, were on the average 8 per cent higher than SA-1 or SA-2. Flight-determined values of normal force and center of pressure location generally agreed well with predicted data. Deviations were within the telemetry error margins. The vehicle was statically unstable, with the most aft center of pressure location during the transonic regime being at approximately 1.2 calibers forward of the center of gravity.

Pressure measurements made at the base of the vehicle and around the fuel and LOX containers of the S-I stage generally agreed well with wind tunnel data. Aft of the shoulder of the Jupiter nose cone and the 45 degree flare of the S-I/S-IVD interstage of SA-4, steady-state pressure measurements from flight were somewhat lower than wind tunnel values at transonic Mach numbers. A minimum surface pressure coefficient of -1.74 was observed at Mach 0.7, one inch behind the Jupiter nose cone shoulder of SA-3.

The interstage area of SA-4 was modified to simulate the 45 degree flare and the various protuberances to be flown in subsequent Saturn I, Block II vehicles. Local steady-state and fluctuating pressure measurements were made in this area, which is basically a separated flow region. The maximum pressure forward of the flare occurred in the transonic regime; a maximum C_p of 0.6 was observed at Mach 1.1 for the near-zero angles-of-attack.

The I-beam end protuberance in the vicinity of the 45 degree flare apparently, because of the formation of local shock waves aft of its wedge-shaped portion, produced

a localized region of high pressure fluctuations and aerodynamic noise. Root-mean-square pressure fluctuations, in the order of 19 per cent of the free-stream dynamic pressure, were observed in this vicinity. Power spectral densities obtained from three measurements showed a predominance in frequencies in the range between 50 and 300 cycles per second.

INTRODUCTION

The Saturn I, Block I R&D program was comprised of four flight test vehicles – SA-1 through SA-4. These early flight configurations each consisted mainly of an 8-engine clustered booster (S-I) stage, dummy upper stages (S-IVD and SVD), and a Jupiter nose cone. On the subsequent Block II configuration, fins will be added to improve the aerodynamic stability characteristics. A live S-IV upper stage will also be incorporated into the Block II phase of the R&D program. The Saturn I operational vehicle will carry the Apollo payload into Earth orbit.

References 1 through 4 contain results of the Early Engineering Evaluation of each of the four Block I test vehicles. Here, the performance of each major vehicle system is discussed with special emphasis on malfunctions and deviations. The first four Saturn flights were each a complete success.

This report contains a more detailed presentation of the aerodynamic evaluation of SA-1 through SA-4 as pertaining to axial force calculations, stability analysis, environmental steady-state and fluctuating pressure data, and aerodynamic noise measurements.

The attainment of narrower error margins and, subsequently, more accurate aerodynamic stability data from flight depends largely on relatively high values of dynamic pressure and angle-of-attack. When compared with the other three Saturn test flights, SA-3 had relatively lower values of dynamic pressure, while SA-4 angles-of-attack generally oscillated about zero degrees. Apparently for this reason, no reliable aerodynamic stability data were obtained from SA-3 or SA-4. One of the possible benefits of a 7-engine tilt program, therefore, is the ability to obtain more adequate stability information from flight as a consequence of the increased angle-of-attack.

Aerodynamic and base heating investigations are not considered in this report. For the first four Saturn flights, these investigations were performed by the Aero-dynamic Analysis Branch, Aeroballistics Division and by the Propulsion Branch of Propulsion and Vehicle Engineering Division. Some results from these analyses may be found also in References 1 through 4. Subsequent aerodynamic reports on future Saturn flight test vehicles, prepared by the Flight Evaluation Branch, will contain aerodynamic heating information.

I. SATURN I, BLOCK I CONFIGURATION

The first four Saturn flight vehicles (SA-1 through SA-4) comprised the Saturn I, Block I R&D program. As shown in Figures 1 and 2, the external configuration of all four vehicles was basically the same except SA-4 which was modified to simulate the Saturn I, Block II interstage area. In addition, the Jupiter nose cone was elongated 32.57 inches on SA-4 to accommodate a Q-ball angle-of-attack meter.

II. AERODYNAMIC TRAJECTORY

Figure 3 shows telemetered pitch and yaw angles-of-attack versus Mach number for each of the Saturn flights. By definition, a positive pitch and yaw angle-of-attack brings the fin I and II positions, respectively, on the windward side of the velocity vector. Except for SA-4, all vehicles showed a pitch angle-of-attack variation between +2 and -6 degrees between Mach 0.4 and 3.2, and the yaw angle-of-attack did not exceed ±2 degrees during this same Mach number interval. The SA-4 trajectory, because of a changed tilting program, was such that both the pitch and yaw angles-of-attack generally oscillated about zero degrees.

Because of the heavier liftoff mass of SA-3, which resulted from a full propellant loading, its trajectory was markedly different from that of the other three Saturn flights. This difference in trajectory was manifested by the lower values of ambient pressure, dynamic pressure, and Reynolds number seen in SA-3 at comparable Mach numbers. Figure 4 shows Reynolds number, based on 257-inch (6.528 m) reference body diameter, as a function of Mach number for the Saturn flights.

At Mach 1.4, a maximum dynamic pressure of 0.29 kg/cm^2 was observed for SA-3. A maximum dynamic pressure of approximately 0.37 kg/cm^2, occurring at around Mach 1.5, was generally observed for the other three Saturn flights.

III. AXIAL FORCE AND AERODYNAMIC STABILITY
PARAMETER ANALYSIS

Axial force and stability parameters were determined from measured data and comparisons have been made with predicted (wind tunnel) results. Figure 5 is a sketch showing the axial and normal forces acting on the vehicle, angle-of-attack conventions, and the equations used to compute the various aerodynamic coefficients from telemetered data.

A. AXIAL FORCE COEFFICIENT

The axial force coefficient was determined by the Flight Simulation Section, Flight Evaluation Branch, by a method whereby the "telemetered" thrust * and mass flow rates are adjusted to fit a simulated trajectory to the reference tracking trajectory (Ref. 5). This is accomplished by assuming the "telemetered" thrust and mass flow rates as the first approximation and computing a preliminary trajectory. Through partial derivatives from the actual post-flight trajectory, new values of thrust and mass flow rates are obtained. With these new values of thrust and mass flow rate, C_X is determined by the relation

$$C_X = \frac{F - ma_L}{qS} \tag{1}$$

By alternately solving for thrust and mass flow rate, the procedure above is repeated until the simulated trajectory converges to the reference tracking trajectory, which in each case gives a new value of C_X from Equation 1. Because of poor tracking data, it was not possible to obtain a C_X curve for SA-3.

Figure 6a is a plot of axial force coefficient versus Mach number for SA-1 and SA-2 as determined from flight measurements. Also shown are predicted values from Reference 6. Axial force values for these two flights were, for all practical purposes, identical. As shown in the figure, the axial force coefficient was roughly 15 per cent less than predicted for Mach numbers above 0.7.

Figure 6b shows the flight-determined C_X for SA-4. From Mach 0.6 to 2.8, the power-on C_X for SA-4 was on the average 8 per cent higher than SA-1 or SA-2. This slight increase in C_X was expected because of the added protuberances and interstage modifications. A close examination of the curves in Figure 6 reveals that the predicted C_X for SA-4 shows values less than the predicted of SA-1 or SA-2. The predicted power-on axial force is determined by adding a power-on base drag component to the experimentally determined fore-drag component (power-off). This deviation in original predicted values is caused by the fact that results from wind tunnel hot-jet power-on tests were not available at the time the prediction was made. Consequently, theoretical predictions of power-on base drag were made by using Jupiter flight test data which turned out to be somewhat higher than values obtained from the subsequent hot-jet wind tunnel model tests of SA-1.

Theoretical and wind tunnel analyses have shown that the angle-of-attack influence on axial force may be neglected for total angles-of-attack under 15 degrees, which, as shown in Figure 3, was the case for all Saturn Block I flight tests.

---

* Thrust derived from telemetered engine chamber pressures.

4

B. GRADIENT OF NORMAL FORCE COEFFICIENT

The gradient of the normal force coefficient ($C_{z\alpha}$ or C_z') was obtained using telemetered values of angle-of-attack, normal acceleration and engine deflection;

$$C_z' = \frac{m \ddot{\gamma} - \Sigma F_0' \beta}{q S \alpha} \qquad (2)$$

where

$$\Sigma F_0' \beta = F_1' \beta_1 + F_2' \beta_2 + F_3' \beta_3 + F_4' \beta_4 = \text{total normal thrust component}$$

Figure 7 is a plot of C_z' versus Mach number obtained from SA-1 and SA-2. Flight results generally agreed well with predicted values in the supersonic regime. C_z' for SA-2 reached a maximum value of approximately 3.3 at Mach 1.15 compared with a predicted value of 3.1 at Mach 1.0. The SA-1 curve had a peak value of 3.7 at Mach 1.1 which seems questionable. Unfortunately, because of the lower dynamic pressure values of SA-3, it was not possible to obtain equally reliable data either to support or disqualify this observation.

C. CENTER OF PRESSURE LOCATION

The center of pressure of the vehicle was computed through the relationship

$$CP/D = CG/D + 1/C_z' q S \alpha D \ [\Sigma F_0' \beta \ (CG) + I \ddot{\varphi} + D_t \dot{\varphi}] \qquad (3)$$

using the smoothed values of C_z' from Figure 7.

Values of CP/D for SA-1 and SA-2 obtained from Equation 3 are plotted versus Mach number in Figure 8 together with predicted values. The forward movement of the center of gravity because of propellant consumption is also shown in the figure. Results from SA-1 and SA-2 show good agreement with predicted values. The most aft flight-derived location of the center of pressure during the transonic regime was observed to be around 3.6 calibers forward of station 100 (approximately 1.2 calibers ahead of the C. G.) and occurring at Mach 1.2. Near Mach 2.0, both flights showed a maximum forward center of pressure location of approximately 4.3 calibers from the gimbal plane.

D. GRADIENT OF MOMENT COEFFICIENT ABOUT C. G.

The gradient of the moment coefficient about the center of gravity was obtained from the relationship

$$C_{m_\alpha} = C_z{'} \, (CP/D - CG/D) \hspace{4cm} (4)$$

where the values of $C_z{'}$ and CP/D are those in Figures 7 and 8, respectively. Values of C_{m_α} for SA-1 and SA-2 are shown as a function of Mach number in Figure 9 together with the predicted curve. The vehicle is statically unstable during the entire portion of the trajectory. As shown in Figure 9, values of C_{m_α} obtained from both flights agree reasonably well with each other and also with those predicted.

E. DATA REDUCTION AND ERROR ANALYSES

A probable error band was determined for the aerodynamic stability curves based upon individual expected error values assigned to telemetered readings of angle-of-attack, normal acceleration, angular velocity, and engine deflections. The error margins for $C_z{'}$, CP/D, and C_{m_α}, which were arbitrarily referenced to the SA-2 curves, are computed by taking the root-mean-square value of the total error determined through the use of partial derivatives. The small values of yaw angle-of-attack and subsequently low normal accelerations on SA-1 and SA-2 confined the stability analysis to the pitch plane only.

Because of the uncertainty in the errors associated with the iteration procedure used for the engine performance evaluation, it was felt that it may be difficult to estimate accurately the absolute error in the axial force coefficient, C_X, which is a by-product of the engine evaluation. For this reason, the percentage variation in the axial force coefficient observed from Jupiter ballistic missile flights (Ref. 7) has been used to determine the probable error bands in C_X. However, the close agreement between the SA-1 and SA-2 curves indicates that the reliability may be greater than indicated by these error margins. An error analysis performed by the Flight Simulation Section, Flight Evaluation Branch, also supports this. The improvement over the results obtained for the Jupiter flights is because of improvements in the engine performance evaluation program. Data from predicted and SA-1 fell within the error bands determined by SA-2 values.

IV. STEADY-STATE PRESSURE MEASUREMENTS

Figure 10 is a table showing the location, description, and the manufacturer of the various pressure instruments which were used in the Saturn flights. Except for two strain gauge transducers and two acoustic microphones mounted on the S-I/S-IVD interstage of SA-4 (shown in Figure 20) all transducers were pneumatic-type pressure responsive capsules which actuated linear potentiometers. These were used mainly to measure local steady-state pressures. Frequency response tests made on this type of instrument (Ref. 8) indicate low dynamic sensitivity after 20 cps.

6

A low-pass digital filter was used to smooth the raw steady-state telemetered pressures. Based upon previous experience, a telemetry error margin of approximately ± 0.018 kg/cm^2 (± 0.25 psia) was assigned to the data from the individual measurements.

A. BASE PRESSURE

The heat shield in the Saturn flights was instrumented with three absolute base pressure measurements. Figure 11 is a band showing base pressure coefficient versus Mach number. The band represents the maximum variation of each and all measurements in the four flights. On the average, base pressures from SA-3 and SA-4 were relatively higher than the two previous flights and compose the upper limits of the band. At approximately Mach 1.7 and thereafter, telemetered data from all flights showed pressure values higher than ambient. This positive pressure thrust at higher altitudes is attributed to the interaction of the strongly expanding exhaust jets which force part of the exhaust gases to flow backward towards the base. In the transonic and supersonic regime, a minimum base pressure coefficient of approximately -0.2 was observed at Mach 1.1.

Also shown in Figure 11 are wind tunnel test data from References 10 and 11. These wind tunnel tests approximated the flight trajectory of SA-1 by simulating the Mach number and static pressure at altitude. Telemetered flight results generally agreed well with wind tunnel data except in the low supersonic regime where flight results were more positive. Wind tunnel tests (Refs. 9 and 10) have shown that during certain portions of the trajectory, the base pressure generally increases with a decrease in ambient pressure when the Mach number is held constant. Therefore, it appears that this deviation between flight and wind tunnel data is caused by the trajectory.

The base drag coefficient of the vehicle was calculated using a mean value of the pressure readings observed on the heat shield.

$$C_{Db} = - (C_{Pb})_{avg.} \frac{S_B - S_{BN}}{S} \tag{5}$$

where

$$\frac{S_B - S_{BN}}{S} = 0.7 \text{ (effective base area correction factor to account for all nozzle exit areas)}$$

Figure 12 is a band showing the maximum variation of C_{Db} for all flights. Based upon the maximum values of C_{Db} shown in Figure 12 and the values of C_x in Figure 6, base drag constitutes about 35 per cent of the total axial force on the vehicle at Mach 0.2, but only 10 per cent at Mach 1.2 and about 6 per cent at Mach 1.5.

B. PRESSURE MEASUREMENTS ON BOOSTER-TANK AREA

1. _Station 205._ Four local static pressure gauges were located on the fillets of the flared-out region on intermediate points adjacent to the extreme lower portion of the fuel and LOX tanks. This area is actually a tapered, scalloped region in which succeeding cross sections between the fuel and LOX tanks alternate between a concave and convex surface. Figure 13 shows a band of pressure coefficients versus Mach number obtained from these measurements.

Since each pair of measurements shown in Figure 13 is diametrically opposite one another, the bands shown represent the pressure variations for pitch angles-of-attack in a range of ± 6 degrees. A comparison between Figures 13a and 13b shows that measurements D77-10 and D79-10 located on the convex surface showed higher pressures than those on the concave surface (D76-10 and D78-10). A maximum pressure coefficient of 0.4 was observed at Mach 1.6 (Fig. 13b).

Flight results showed good agreement with wind tunnel test data, Reference 12. These wind tunnel measurements were made on the tanks and not on the actual fillets. Pressures for the most part were higher than ambient in all flights, as expected. The negative portion of the band in Figure 13a is contributed by measurement D78-10 in SA-2 and SA-3. Here, the negative C_p values may have been caused by the relative rearward movement of the windward separation shock wave with respect to the pressure orifice on the fillet. Since this phenomenon appears to have occurred in several other locations on the Saturn, it will be discussed in more detail in Section D.

2. _Stations 860 and 863._ Figures 14 and 15 are bands of pressure coefficient versus Mach number from measurements made at stations 860 and 863 on and around the fuel containers. Pressure gauges for measurements D81-F1 and D83-F3 at station 860 were located on the skin of fuel containers 1 and 3, respectively, facing the center of the cluster. Measurements D80-F1 and D82-F3 were also located on fuel containers 1 and 3, but the orifices were located on the end ring frame of the containers facing the flight direction. The locations of these measurements are shown in sketches in Figures 14 and 15.

Negative pressure coefficients were observed at stations 860 and 863, as expected. Because the flow has expanded around the station 867.3 corner of the adapter section, these measurements may be considered to be in a local "base pressure" region. A minimum C_p value of -0.2 at Mach 1.1 was observed at station 860; at station 863, a minimum C_p reading of -0.3 was observed at Mach 1.06.

From the relatively narrow bands of data shown in the figures, it appears that this region was not influenced significantly by angle-of-attack changes. On the average, flight results were generally more positive than the wind tunnel data of Reference 13.

8

C. SURFACE PRESSURES, SA-3 DUMMY PAYLOAD

The dummy payload stage of the SA-3 vehicle was modified by the installation of two aluminum panels, 2.31 cm thick, each extending on a 60 degree circumferential area from station 1731 to 1699. On the area encompassed by the panels, the shoulder was faired back to station 1727. The panels were then instrumented with longitudinally spaced surface pressure measurements as part of an experiment to simulate a portion of the shoulder configuration on the nose fairing of Centaur F-1. Telemetered flight data from five of these measurements (located 65 degrees off fin location III towards IV) are presented herein and comparisons made with wind tunnel and theoretical results. A more detailed presentation of the purpose and results of the above experiment is given in Reference 8.

Figure 16 shows the surface pressure distribution (C_p versus station) between stations 1726 and 1701 at various Mach numbers. These pressure orifices were on the windward side of the velocity vector. Figure 17 presents plots of surface pressure coefficient versus Mach number for three of these measurements. At Mach 0.7, measurement D152-30, located one inch behind the shoulder, displayed the lowest pressure reading – a minimum C_p value of -1.74 (Figs. 16b and 17a). Evidence of the downstream movement of the lambda-type shock wave with increasing Mach number was indicated by the sudden telemetry drops experienced by the various measurements at different flight times. This sudden drop in local surface pressure was first detected at Station 1726, at Mach 0.65.

Flight results generally agreed well with wind tunnel data of References 12 and 14. At Mach 0.7 and thereafter, C_p values from SA-3 are slightly less negative than wind tunnel data of Reference 14 on the area immediately behind the shoulder.

D. INTERSTAGE SURFACE PRESSURE MEASUREMENTS

1. SA-3 Interstage. The S-I/S-IVD interstage area was instrumented with four steady-state pressure measurements. The four orifices were located in pairs at stations 989.3 and 1019.3, diametrically opposite one another in the pitch plane. Figure 18 shows pressure ratios, P_s/P_a, versus Mach number for the two leeward side measurements, while the windward side measurements are shown in Figure 19. Angle-of-attack effects indicated by higher pressures on the windward than on the leeward side were observed at station 989.3 (Figs. 18a and 19a) up to Mach 2.2. The same pitch angle-of-attack effect is observed at station 1019.3 but only up to Mach 1.2 after which pressures from measurement D85-20 on the windward side fell to near-ambient values.

The measurements above are presumably in an area of flow separation which is marked by the formation of a strong shock wave ahead of the 24 degree flare on the SA-3 vehicle. Experimental studies on cylinder-cone-flares (for example, Ref. 15) have shown a large forward movement of the leeward separation point (and associated shock

wave) with a thickening of the turbulent boundary layer; conversely, a slight aft movement of the windward separation point has been observed together with a slightly thinned boundary layer. The sudden drop in pressure experienced by data from the windward measurement D85-20 was most likely due to the downstream movement of the flare shock wave relative to the pressure orifice at higher Mach numbers.

When the data were converted to pressure coefficient form, C_p, the maximum values for each measurement all occurred at approximately Mach 1.1; the maximum observed C_p value was 0.71, obtained from windward measurement D84-20 at station 989.3. Wind tunnel test data (Ref. 12) also shown for comparison in Figures 18 and 19, showed pressure readings somewhat lower than those telemetered from flight.

2. _SA-4 Interstage._ The major modifications to the SA-4 vehicle consisted mainly in adding dummy retro rockets, I-beam end-fairings, ullage rocket fairings, hydrogen chilldown ducts and cable tunnel to the S-I/S-IVD interstage area to simulate the Block II configuration. In addition, a 45 degree flare was incorporated. To measure the full-scale effects of protuberances and the 45 degree flare on the local aerodynamic characteristics of the interface region, a total of 10 pressure measurements were installed between stations 975 and 1064, near fin location I. Of these, two were high frequency response Statham strain gauge transducers intended for measuring fluctuating pressures. To measure the aerodynamic noise in the boundary layer, two acoustic microphones were also installed in the general vicinity of these measurements. Figure 20 is a sketch of the S-I/S-IVD interstage area of SA-4 with a table showing the location and general characteristics of each measurement.

Figure 21 presents plots of surface pressure ratio, P_s/P_a, versus Mach number for data from each individual measurement. An increase in pressure was generally observed with proximity to the 45 degree flare, as has been observed previously in experimental studies of flare-induced separation.

Interpolated wind tunnel data (Ref. 16), obtained from a 0.778 per cent scale smooth model of the Saturn I, Block II configuration, are shown for comparison in the graphs. SA-4 flight results are generally higher than wind tunnel data for those surface stations forward of the 45 degree flare.

A minimum surface pressure ratio of 0.12 was observed from measurement D162-11, station 977.3, at Mach 0.97 (Fig. 21i). This pressure ratio corresponds to a surface pressure coefficient of -1.34. Pressures obtained from measurement D161-11 at station 975.3, as expected, were higher because of increasing distance downstream of the shoulder. Wind tunnel data (scaled to station 975), shown for comparison in Figures 21 (i, j), show that between Mach 0.9 and 1.1 telemetered flight readings of P_s/P_a were lower than wind tunnel data by a factor of 1.7 to 2.1. At Mach 1.4 and thereafter, good agreement was observed between flight and wind tunnel data for measurement D161-11. However, the agreement of measurement D162-11, at station 977.3 just after the flare, was not as good.

Measurements D164–20 and D159–20, which were located symmetrically on opposite sides of the I-beam fairing, showed very nearly the same pressures up to Mach 1.6 indicating a symmetrical flow. This is as would be expected since the angle-of-attack (yaw) was small.

Figure 22 shows plots of C_p versus SA-4 vehicle station at various Mach numbers. The data were obtained from the eight measurements located nearly in line from station 1064.3 to 975.3 on the fin II side of the I-beam fairing (Fig. 20). These results are the same information as presented in Figure 21(a–j) but in a different form.

Analysis of the data revealed that the maximum pressure distribution, as in SA-3, occurred near Mach 1.1. At this Mach number (Fig. 22c), a maximum C_p of 0.6, which was 50 per cent above the value obtained in the wind tunnel, was observed between stations 989.3 and 1019.3. Locations of the pressure orifices on the wind tunnel model were scaled to SA-4 stations using calibers from station 979.3 as a reference point.

The raw telemetered data from measurement D159–20 and D163–20, the two strain gauge transducers, displayed a gradual drop in absolute pressure level after M = 2.0, which does not appear to be valid. The sensing element, or diaphragm, of the strain gauge transducers, unlike the potentiometer-pneumatic systems, are flush-mounted to the vehicle surface. Heat measuring transducers located in this general vicinity showed an increase in temperature at this Mach number (Ref. 4). The most likely explanation for the deviation shown by the strain gauges is that the sensing element was affected by the rise in aerodynamic heating rate in this vicinity. Laboratory tests seem to support this conclusion.

The low frequency pressure oscillations observed on the data from the two measurements behind the shoulder, Figure 21(i,j), appear to be angle-of-attack effects in yaw stemming mainly from the I-beam fairing. As shown in Figure 20, measurements D159–20 and D163–20 are located on opposite sides of the I-beam fairing, D159–20 being on the leeward side of the fairing for positive yaw angles-of-attack. Between Mach 1.4 and 1.8, a variation in pressure was observed in phase with the yaw angle-of-attack oscillations. However, an opposite pressure effect was seen in data from both measurements in that the pressure decreased when the tap was on the windward side and increased when it was on the leeward side.

The surface-to-ambient pressure ratio for measurements D87–20 at station 1019.3 (Fig. 21d) did not exhibit the same slope in its upward trend as was observed after Mach 2.0 from measurements nearby. At Mach 2.99, C_p values for measurement D87–20 were, on the average, about 35 per cent lower than flight data from two measurements located longitudinally on either side. This may be a localized effect produced by the I-beam fairing or because of measurement inaccuracies.

V. FLUCTUATING PRESSURE AND AERODYNAMIC NOISE MEASUREMENTS

Some results from a digital power spectral density (PSD) analysis made on data from measurement D159-20, the high-frequency response strain gauge transducer on SA-4, are shown in Figures 23 to 25.[*] Figure 23 shows power spectra curves for several flight intervals of 2-second duration. The filter bandwidth used for this analysis was 10 cps with a sampling rate of approximately 850 samples per second.

The maximum power was observed between 70 and 72 seconds of flight (Fig. 23d) where a peak value of 0.011 psi^2/cps [52.3x10^6 (dynes/cm^2)^2/cps] was observed for a frequency of 205 cps with a secondary peak of 0.0082 psi^2/cps [39x10^6 (dynes/cm^2)^2/cps] occurring at 235 cps. The integral of the power spectrum determines the mean-square value. Figure 24 is a plot of the overall or composite root-mean-square pressure fluctuation about the mean obtained from the relation

$$SPL = 20 \log_{10} \left(\frac{\bar{P}}{\bar{P}_r} \right) \qquad (6)$$

where

SPL = sound pressure level in decibels
$\bar{P}$ = overall root-mean-square pressure fluctuation
$\bar{P}_r$ = reference sound level pressure (2.94 x 10^{-9} psi).

A maximum value of approximately 169.5 db was observed in the interval between 70 and 72 seconds of flight which decreased to 167 db between 77 and 79 seconds. Figure 25 shows $\Delta C_{p(rms)}$ (ratio of overall rms value of fluctuating pressure about the mean to the free-stream dynamic pressure) versus Mach number. The maximum sound pressure level shown in Figure 24 (169.5 db) corresponds to a $\Delta C_{p(rms)}$ value of 0.188 at Mach 1.85.

Because of flow acceleration and changes in the absolute ambient pressure level with flight time, the local oscillating pressure field in the boundary layer is somewhat of a transient phenomenon. Using intervals of smaller duration with greater sampling rates for statistical analyses enabled the pressure-time series in the SA-4 analysis to approximate more closely a stationary random process, which is a necessary condition for time series to be represented by power spectra.

---

[*] This surface measurement was located at station 1012.3 approximately 15 inches (38 cm) from the I-beam fairing, as indicated in Figure 20.

A similar PSD analysis was performed in Reference 4, with fluctuating pressure data obtained from D159-20, but the intervals were of 4-second duration. Since at comparable flight intervals, the PSD curves presented herein are basically similar to those in Reference 4, it appears that when the data were sampled at intervals of 4-second duration, the slow time-varying absolute pressure mean (approximately 0.25 psi/sec) did not distort the power spectra above 5 cps. It is possible, however, that because of this effect, an overestimate might be made of the overall root-mean-square value. Based upon analyses of the data presently available on measurement D159-20, it appears that this overestimate of $\bar{P}$ did not exceed 5 per cent.

Two flush-mounted acoustic microphones were installed on the surface of the interstage near the I-beam fairing: one 33 degrees off fin location I towards IV at station 1012.3 (L64-20), and the other 22 degrees from fin I towards IV at station 1029.3 (L65-20). The measuring range of each instrument was 145-165 db and the telemetry response 3 kc.

Figures 26 and 27 show the frequency spectrum for measurements L64-20 and L65-20, each at three different time intervals during SA-4 flight. Measurement L65-20 had a maximum power peak of 13.5×10^{-5} psi^2/cps $[0.64 \times 10^6$ (dynes/cm^2)^2/cps] at 125 cps occurring between 47 and 52 seconds. Measurement L64-20 (Fig. 26) displayed two peaks of the same magnitude $[10.7$ psi$^2 \times 10^{-5}$/cps or 0.51×10^6 (dynes/cm^2)^2/cps] at 190 and 235 cps in the interval between 74 and 79 seconds.

A comparison of Figures 23, 26, and 27 reveals that the power spectra level obtained from measurement D159-20 is considerably higher than that obtained independently by any of the two acoustic microphones. Consequently, the SPL obtained from D159-20 was higher than that of the microphones. However, the same predominance in frequencies (between 50 and 300 cps) was observed by all three measurements. Between 70 and 80 seconds, particularly, two distinguishable peaks were observed by both measurement D159-20 and L64-20 at frequencies near 190 and 240 cps. Measurement L64-20, as D159-20, was located at station 1012.3, but 49 inches (124 cm) away from the latter (Fig. 20). The higher power level associated with measurement D159-20 may be attributed to its proximity to the I-beam fairing, which, because of local unstable shock waves presumably forming aft of its wedge-shaped portion, produces very localized regions of high boundary layer turbulence and aerodynamic noise.

CONCLUSIONS

Analysis of telemetered data for the Saturn I, Block I vehicles indicates the following conclusions:

1. Values of axial force coefficient measured on SA-1 and SA-2 were nearly identical during the powered flight. The axial force coefficient was roughly 15 per cent less than predicted for Mach numbers above 0.7. Between Mach 0.6 and 2.8, flight-determined values of axial force coefficient for SA-4 were about 8 per cent higher than SA-1 or SA-2, as expected.

2. Flight-determined values of the gradient of normal force coefficient agreed well with predicted data in the supersonic regime. C_z' for SA-2 reached a maximum value of approximately 3.3 at Mach 1.15 compared with a predicted value of 3.1 at Mach 1.0. The SA-1 curve had a peak value of 3.7 at Mach 1.1. The center of pressure location determined from flight data agreed well with predicted values. Near Mach 2.0, both flights indicate a maximum forward center of pressure location of approximately 4.3 calibers from the engine gimbal plane (station 100).

3. The heat shield was instrumented with three absolute pressure measurements. During the transonic and supersonic regime, a minimum base pressure coefficient of approximately -0.2 was observed at Mach 1.1. Flight results generally agreed well with wind tunnel data.

4. Telemetered pressure data from measurements located on and around the top of the fuel containers indicate a minimum surface pressure coefficient of -0.3 observed at approximately Mach 1.1. Pressures in this region did not appear to be influenced by angle-of-attack changes of within ± 6 degrees.

5. At Mach 0.7 a minimum pressure coefficient of -1.74 was observed at a point one inch behind the nose cone shoulder on SA-3. Behind the shoulder of the 45 degree flare on the S-I/S-IVD interstage of SA-4, a minimum surface pressure coefficient of -1.34 was observed at approximately Mach 0.97. These peaks in surface pressure coefficient values are considerably lower than those predicted through wind tunnel tests.

6. Surface pressure measurements were located in the vicinity of the cylinder-flare region on the S-I/S-IVD interstage areas of SA-3 and SA-4. The flight measurement forward of the flare were evidently located in a region of flow separation. SA-3 had a relatively smooth contour in this area and a 24 degree flare. To simulate the Block II interstage area, various protuberances were added to SA-4 together with a 45 degree flare. Telemetered pressures indicate a generally higher pressure distribution than was obtained from wind tunnel data on smooth bodies (no protuberances). The maximum loading for either configuration occurred between Mach 1.0 and 1.1. On SA-4, a maximum surface pressure coefficient of 0.6 was observed at Mach 1.1 for free-stream angles-of-attack near zero degrees.

7. Unsteady pressure data were obtained from two acoustic microphones and one fluctuating pressure measurement located on the SA-4 interstage. The fluctuating

14

pressure measurement located next to a surface protuberance (I-beam fairing) showed the highest pressure oscillations, with a maximum noise level of close to 170 decibels at Mach 1.85. The overall root-mean-square pressure fluctuation at this Mach number was approximately 19 per cent of the free-stream dynamic pressure. A frequency analysis made on fluctuating pressure data from each of the three measurements indicates the largest amplitude oscillations in frequencies between 50 and 300 cycles per second.

REFERENCE

1. Saturn Flight Evaluation Working Group, MSFC, Saturn SA-1 Flight Evaluation, MPR-SAT-WF-61-8, December, 1961 (C).

2. Saturn Flight Evaluation Working Group, MSFC, Saturn SA-2 Flight Evaluation, MPR-SAT-WF-62-5, June, 1962 (C).

3. Saturn Flight Evaluation Working Group, MSFC, Saturn SA-3 Flight Evaluation, MPR-SAT-63-1, VOL I and II, January, 1963 (C).

4. Saturn Flight Evaluation Working Group, Results of the Fourth Saturn I Launch Vehicle Test Flight, MPR-SAT-63-6, May, 1963 (C).

5. Jackson, J.W., Propulsion System Evaluation Through Flight Simulation, MTP-AERO-62-9, August, 1962.

6. MSFC Aeroballistics Division, Control-Stability Data Report for Saturn Vehicle SA-1, MTP-AERO-61-39, April, 1961 (C).

7. Weisler, A.C. and Hágood, C.C., Jupiter Summary Report, Volume VI, ABMA Report No. RJ-TR-61-10, June, 1961.

8. Garcia, F.S., Flight Results of Centaur Simulation Pressure Measurements Flown on Saturn SA-3, MTP-AERO-63-16, March, 1963 (C).

9. Parker, J.R. and Gillard, T.J., An Investigation of Base Heating with a 5.47-per cent Saturn SA-1 Booster Model at Mach Numbers 0.8 and 1.15, Rocket Test Facility, AEDC TN-61-134, November, 1961.

10. Dawson, J.G., An Investigation of Base Heating on a 5.47-per cent Scale Model Saturn SA-1 Booster Afterbody at Mach Numbers 1.64 and 3.07, Rocket Test Facility, AEDC TDR-62-9, January, 1962.

11. Lewis Research Center, Preliminary Results Obtained from the 1/27 Scale Saturn Base Heating Tests in the Lewis 8 x 6 Foot Supersonic Tunnel, October, 1961.

12. Windham, J.O., Pressure Distribution Along a 1.6-per cent Scale Model Saturn C-1 Block I Vehicle, MSFC Aeroballistics Division, Aero Internal Note 7-62, March, 1962.

13. Windham, J.O., Results of the Wind Tunnel Investigation of the Tank Loads on a 1.6-per cent Scale Model of the Saturn SA-1 Configuration, MSFC Aeroballistics Division, Internal Note 12-61, August, 1961.

16

REFERENCES (Concl'd)

14. Experimental Projects Section, Aeroballistics Division, MSFC, Transmittal of Wind Tunnel Test Data, Centaur and Centaur/SA-3 Simulation Models (MSFC Project No. P44), February, 1963.

15. Reding, J. P., Separated Flow Effects on the Static Stability of Cone-Cylinder-Flare Bodies, Lockheed Missiles and Space Company, TM 53-40-119, December, 1962.

16. Experimental Projects Section, Aeroballistics Division, MSFC, Results of a Wind Tunnel Investigation to Determine Pressure and Load Distribution over the C-1 Saturn I, Block II Vehicle, M-AERO-E-110-62, September, 1962.

Station
1951.90

13°21'

1854.40

12°32'

1765.77
1731.12
1699.40

120 DIA

Dummy Payload

S-VD

1506.0

15°

1319.37

S-IVD

220 DIA

24°

979.304
934.30

867.3

III

II   IV

I

Fin Positions Viewed From Rear
(Vehicle tilts over Fin I)

257.0 Ref. DIA

S-I

205

Gimbal
Sta. 100

-1.0

FIGURE 1. EXTERNAL CONFIGURATION OF SATURN VEHICLES SA-1, SA-2, and SA-3

18

Station

1984.472

13°21'

1854.40

12°32'

1765.77
1731.12
1699.40

— 120 DIA

Dummy Payload

S-VD

1506.0

15°

1319.37

—220 DIA

S-IVD

979.304

934.30

867.3

III

II ——— IV

I

Fin Positions Viewed From Rear
(Vehicle tilts over Fin I)

257.00 Ref. DIA

S-I

205

Gimbal
Sta. 100

-1.0

FIGURE 2. EXTERNAL CONFIGURATION OF SATURN SA-4

19

FIGURE 3. FREE-STREAM ANGLES-OF-ATTACK VERSUS MACH NUMBER
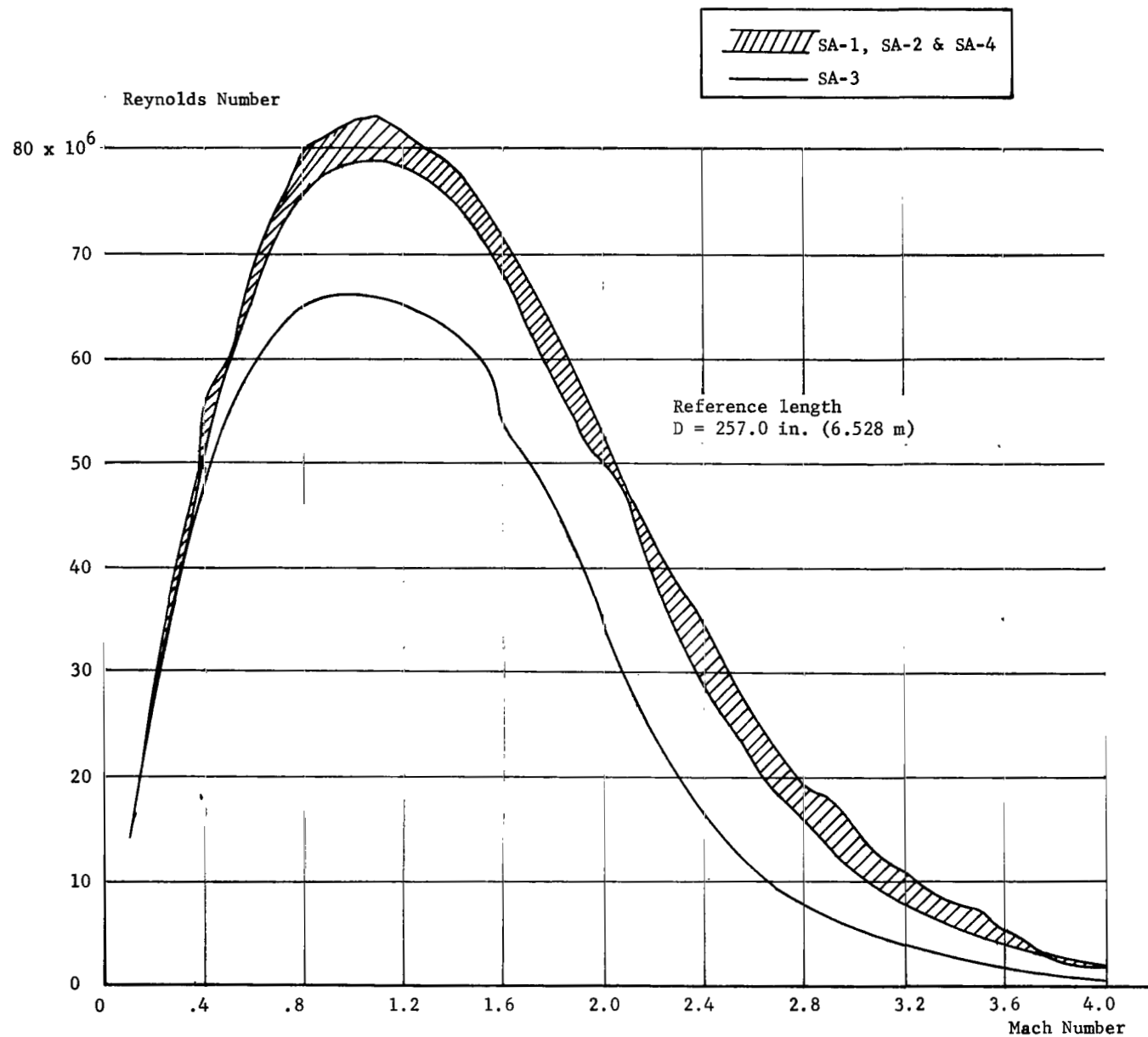
FIGURE 4.   REYNOLDS NUMBER VERSUS MACH NUMBER

$$C_x = \frac{F - m\, a_L}{qS} \qquad \frac{CP}{D} = \frac{CG}{D} + \frac{1}{C_z{}'\,\alpha\, qSD}\left[\Sigma F_o'\beta\ (CG) + I\ddot{\varphi} + D_t\dot{\varphi}\right]$$

$$C_z{}' = \frac{m\ddot{\gamma} - \Sigma F_o'\beta}{qS\alpha} \qquad C_{m\alpha} = \left(\frac{CP}{D} - \frac{CG}{D}\right) C_z{}'$$
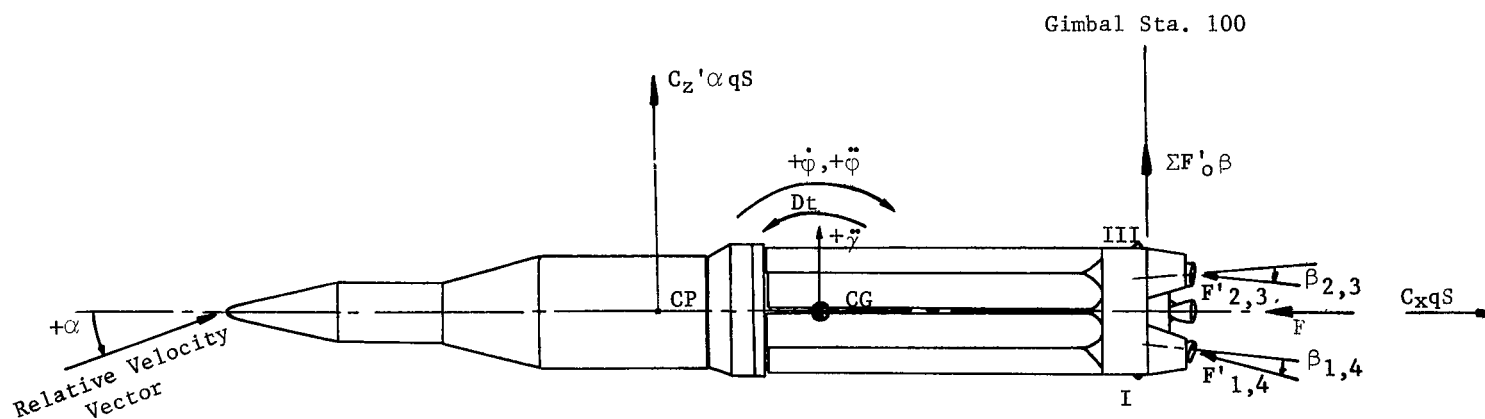
$$\Sigma F_o'\beta = F_1'\beta_1 + F_2'\beta_2 + F_3'\beta_3 + F_4'\beta_4$$

FIGURE 5. SKETCH SHOWING FORCES ACTING ON VEHICLE PLUS STABILITY
EQUATIONS
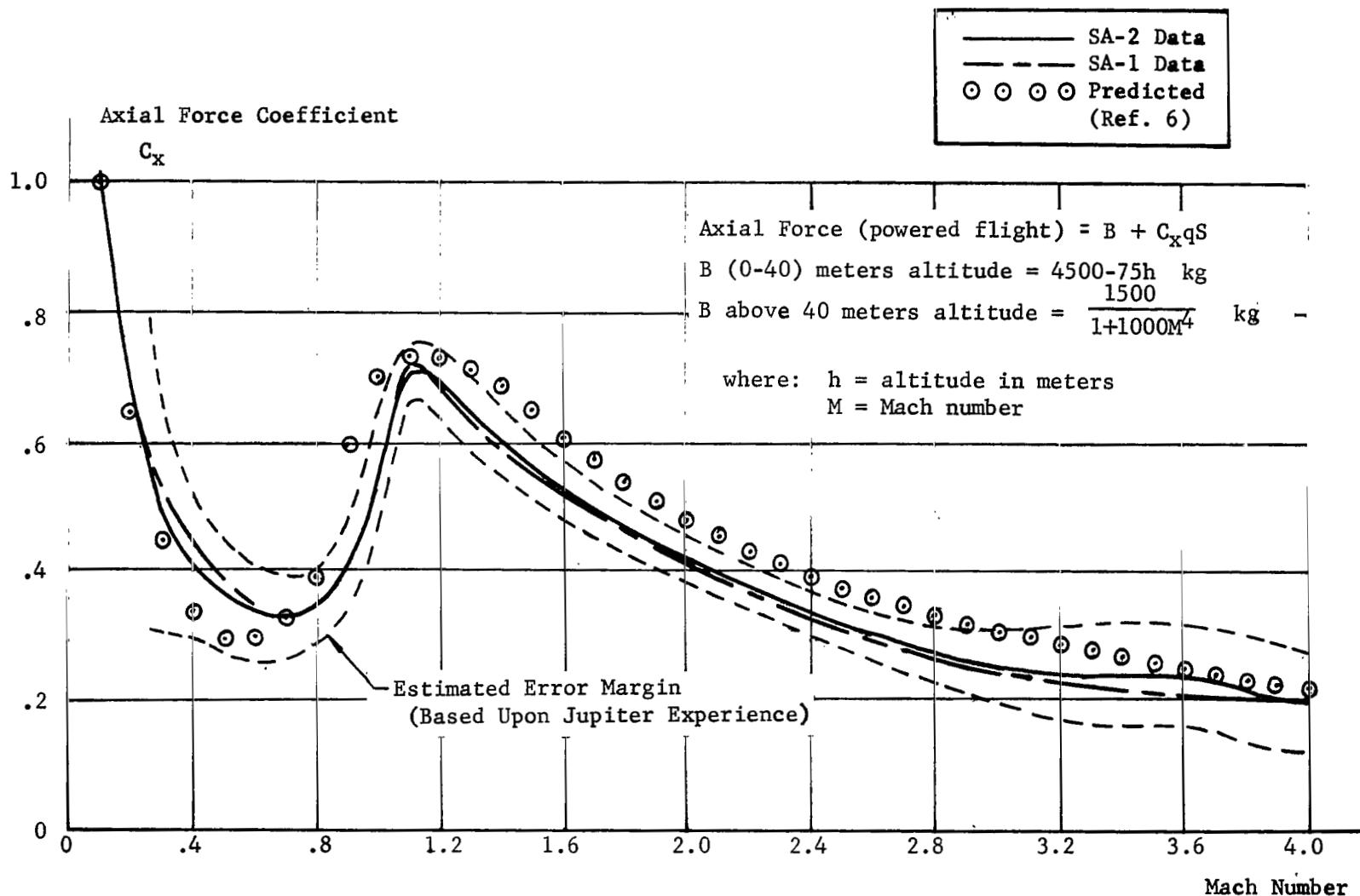
FIGURE 6a. POWER-ON AXIAL FORCE COEFFICIENT VERSUS MACH NUMBER

Axial Force Coefficient

C_X

SA-4 Data

⊙ ⊙ ⊙ Predicted

Axial Force (powered flight) $= B + C_x qS$

B (0-40) meters altitude $= 4500\text{-}75h$ kg

B above 40 meters altitude $= \dfrac{1500}{1+1000M^4}$ kg

where: h = altitude in meters
M = Mach number

Estimated Error Margin
(Based Upon Jupiter Experience)
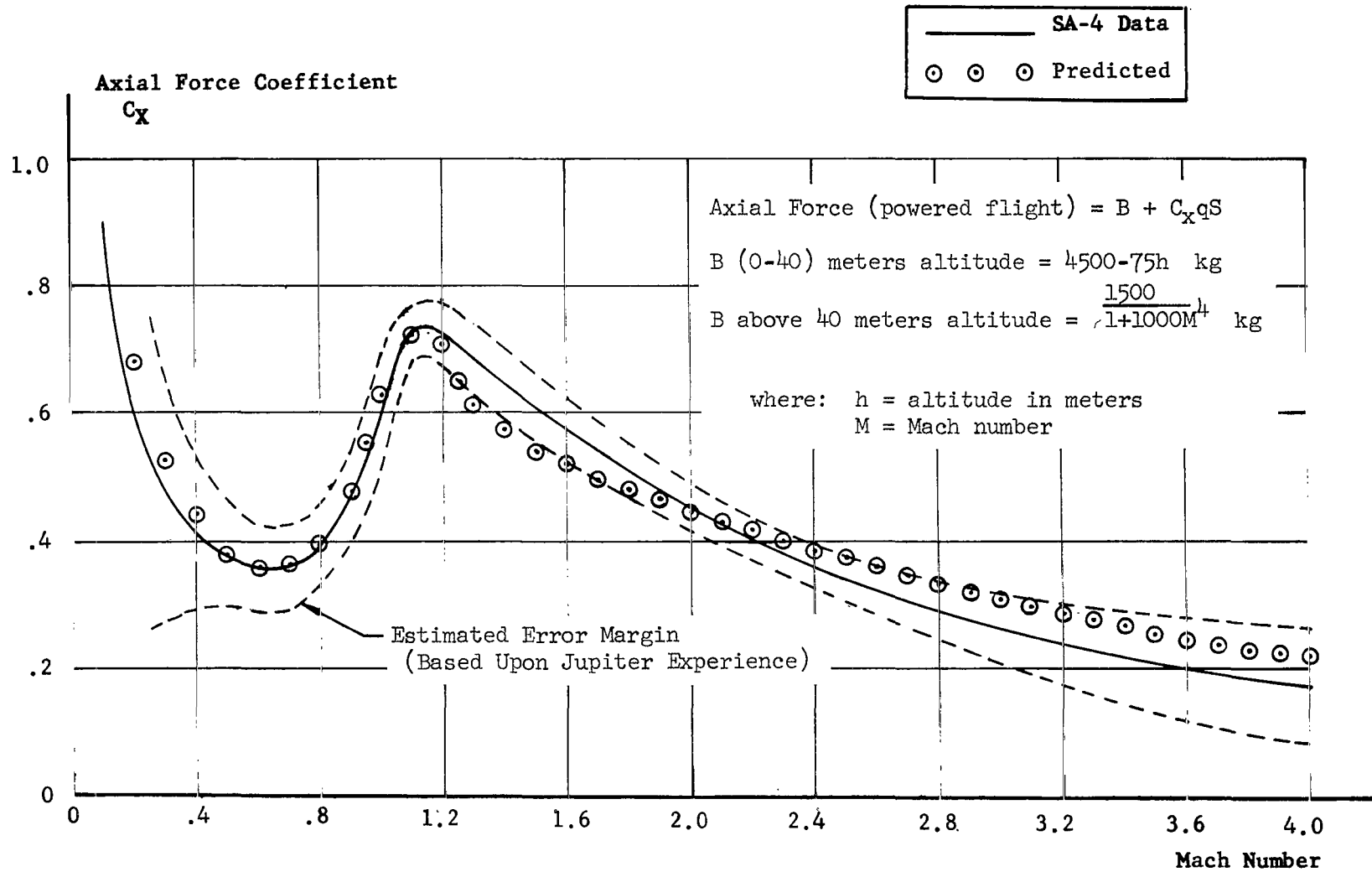
Mach Number

FIGURE 6b. POWER-ON AXIAL FORCE COEFFICIENT VERSUS MACH NUMBER
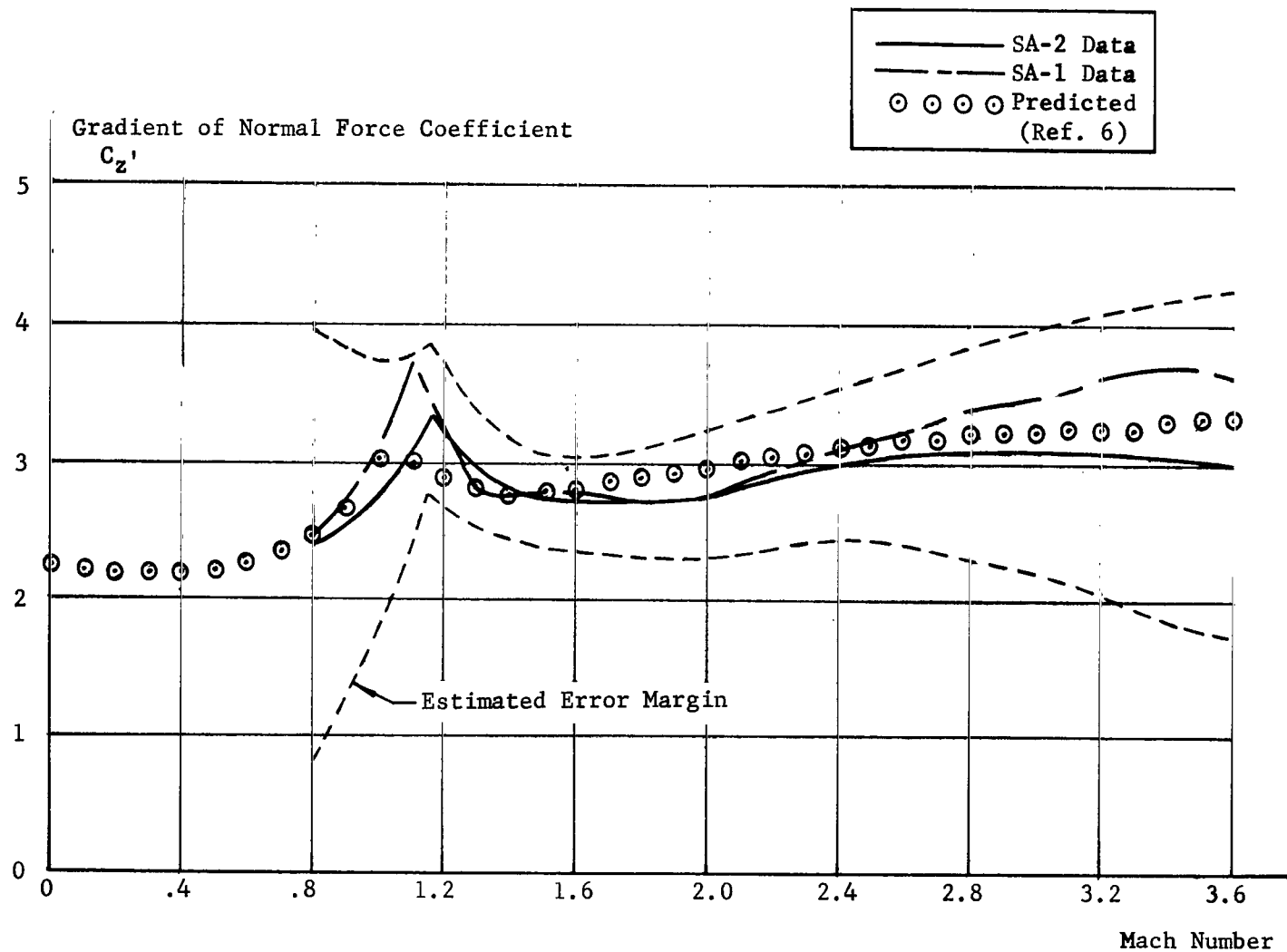
FIGURE 7. GRADIENT OF NORMAL FORCE COEFFICIENT VERSUS MACH NUMBER
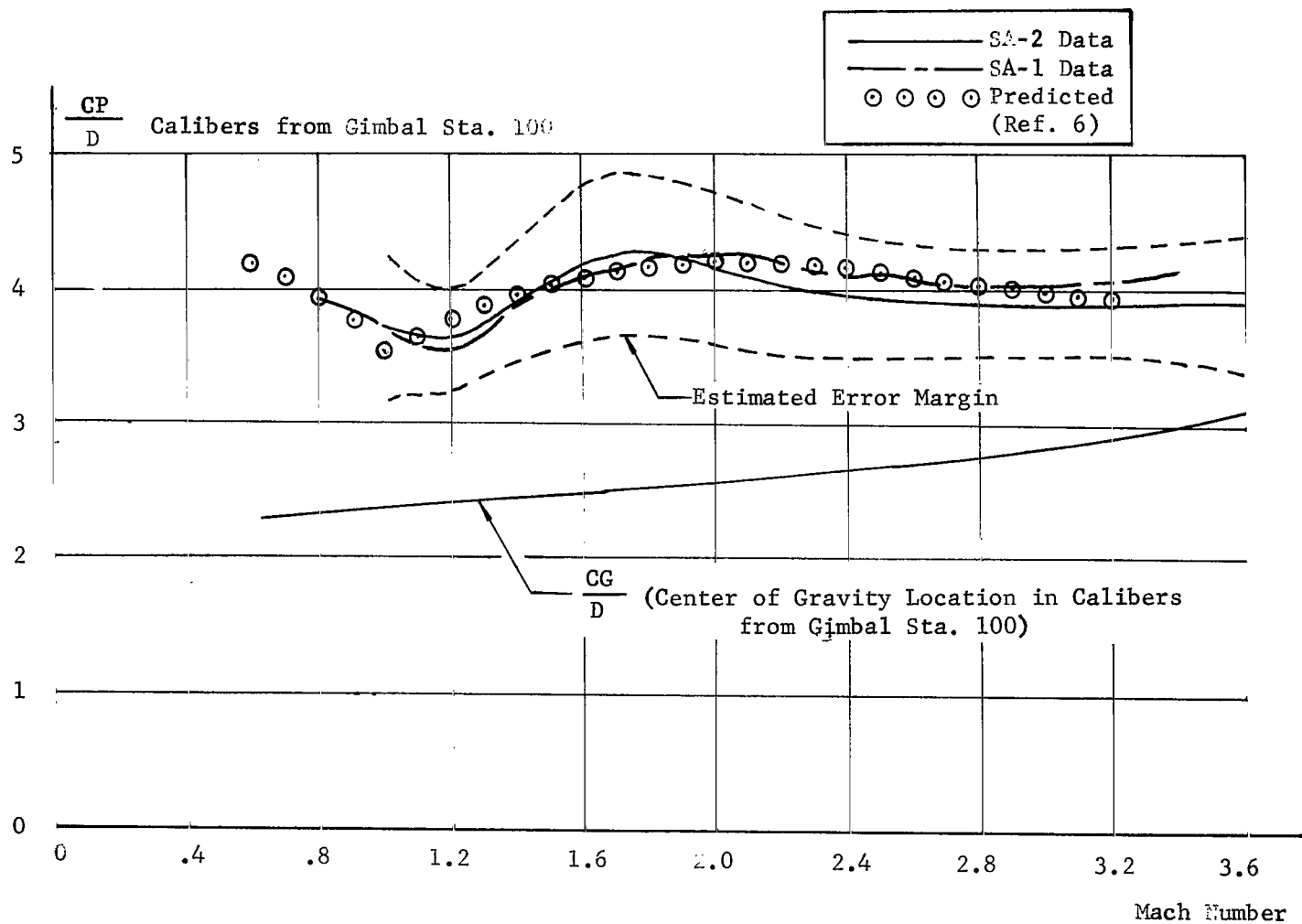
FIGURE 8. CENTER OF PRESSURE LOCATION VERSUS MACH NUMBER
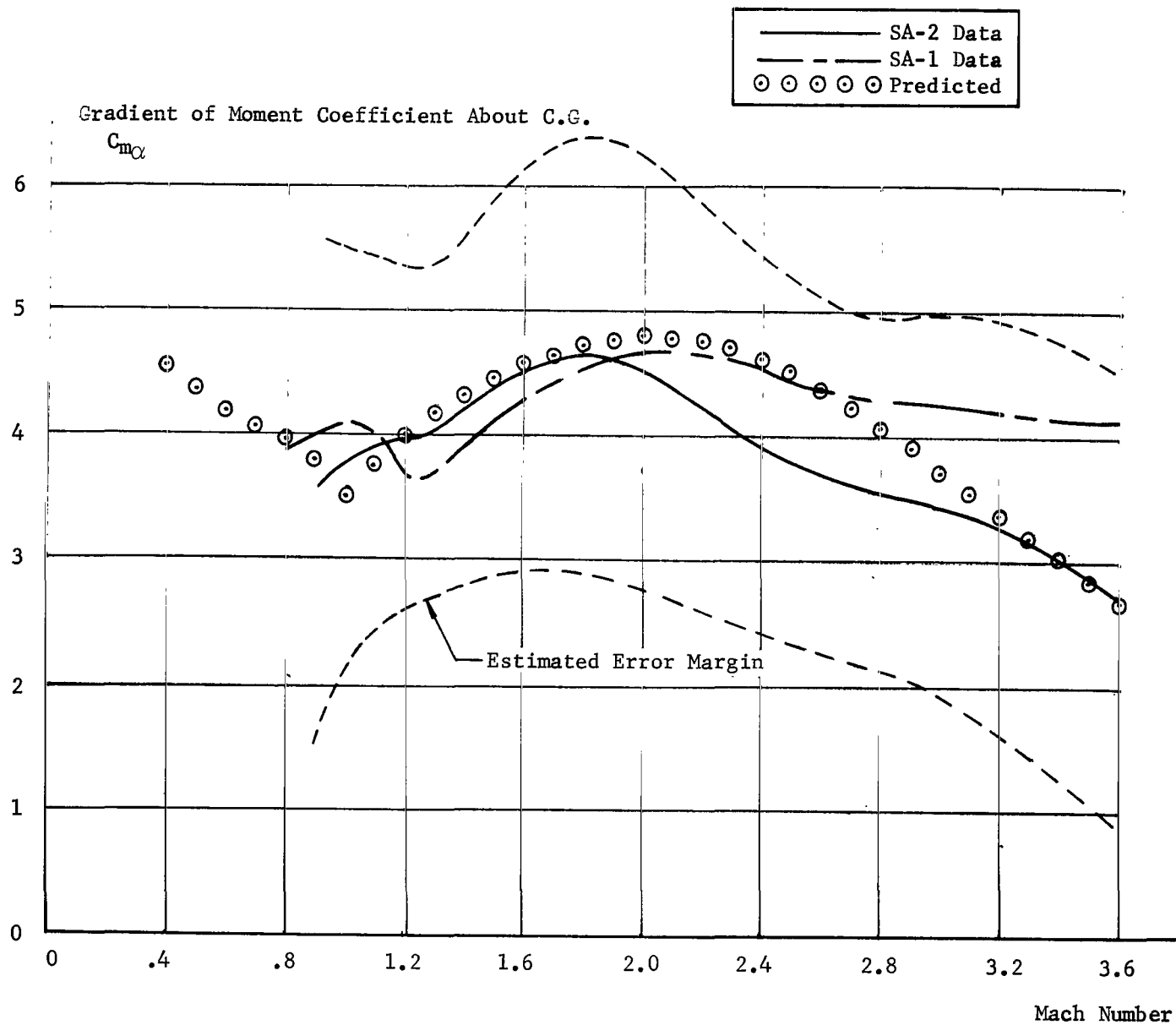
FIGURE 9. GRADIENT OF MOMENT COEFFICIENT ABOUT CENTER OF GRAVITY
VERSUS MACH NUMBER

27

Meas. No.	Location	Vehicle	Range	Manufacturer	Model	Response*
D25-4	Heat Shield	SA-1 thru 4	0-20 psia	Trans-Sonics	2688	C
D25-7	Heat Shield	SA-1 thru 4	0-20 psia	Trans-Sonics	2688	C
D38-4	Heat Shield	SA-1 thru 4	0-20 psia	Trans-Sonics	2688	C
D76-10	Fillets Sta. 205	SA-2	0-20 psia	Trans-Sonics	2688	C
		SA-3 & SA-4	0-25 psia	Servonics	L127-3	
D77-10	Fillets Sta. 205	SA-2	0-20 psia	Trans-Sonics	2688	C
		SA-3 & SA-4	0-25 psia	Servonics	L127-3	
D78-10	Fillets Sta. 205	SA-2	0-20 psia	Trans-Sonics	2688	C
		SA-3 & SA-4	0-25 psia	Servonics	L127-3	
D79-10	Fillets Sta. 205	SA-2	0-20 psia	Trans-Sonics	2688	C
		SA-3 & SA-4	0-25 psia	Servonics	L127-3	
D80-F1	Sta. 863, Top Fuel Tank 1	SA-2	0-20 psia	Giannini	45154SR	C
		SA-3 & SA-4	0-25 psia	Servonics	L127-3	
D81-F1	Sta. 860, Fuel Tank 1	SA-2	0-20 psia	Giannini	45154SR	C
		SA-3 & SA-4	0-25 psia	Servonics	L127-3	
D82-F3	Sta. 863, Top Fuel Tank 3	SA-2	0-20 psia	Giannini	45154SR	C
		SA-3 & SA-4	0-25 psia	Servonics	L127-3	
D83-F3	Sta. 860, Fuel Tank 3	SA-2	0-20 psia	Giannini	45154SR	C
		SA-3 & SA-4	0-25 psia	Servonics	L127-3	
D84-20	Sta. 989.3	SA-3	0-25 psia	Servonics	L127-3	C
D85-20	Sta. 1019.3	SA-3	0-25 psia	Servonics	L127-3	C
D86-20	Sta. 989.3	SA-3	0-25 psia	Servonics	L127-3	C
D87-20	Sta. 1019.3	SA-3	0-25 psia	Servonics	L127-3	C
D152-30	Sta. 1726	SA-3	0-15 psia	Servonics	L158-2	25 cps
D153-30	Sta. 1720	SA-3	0-15 psia	Servonics	L158-2	25 cps
D154-30	Sta. 1714	SA-3	0-15 psia	Servonics	L158-2	C
D155-30	Sta. 1707	SA-3	0-15 psia	Servonics	L158-2	C
D156-30	Sta. 1701	SA-3	0-15 psia	Servonics	L158-2	25 cps

C - Commutated Channel, 10/sec, 2.4 cps maximum telemetry response
* Instrument or telemetry channel, whichever is lower.

FIGURE 10. SATURN I BLOCK I PRESSURE MEASUREMENTS
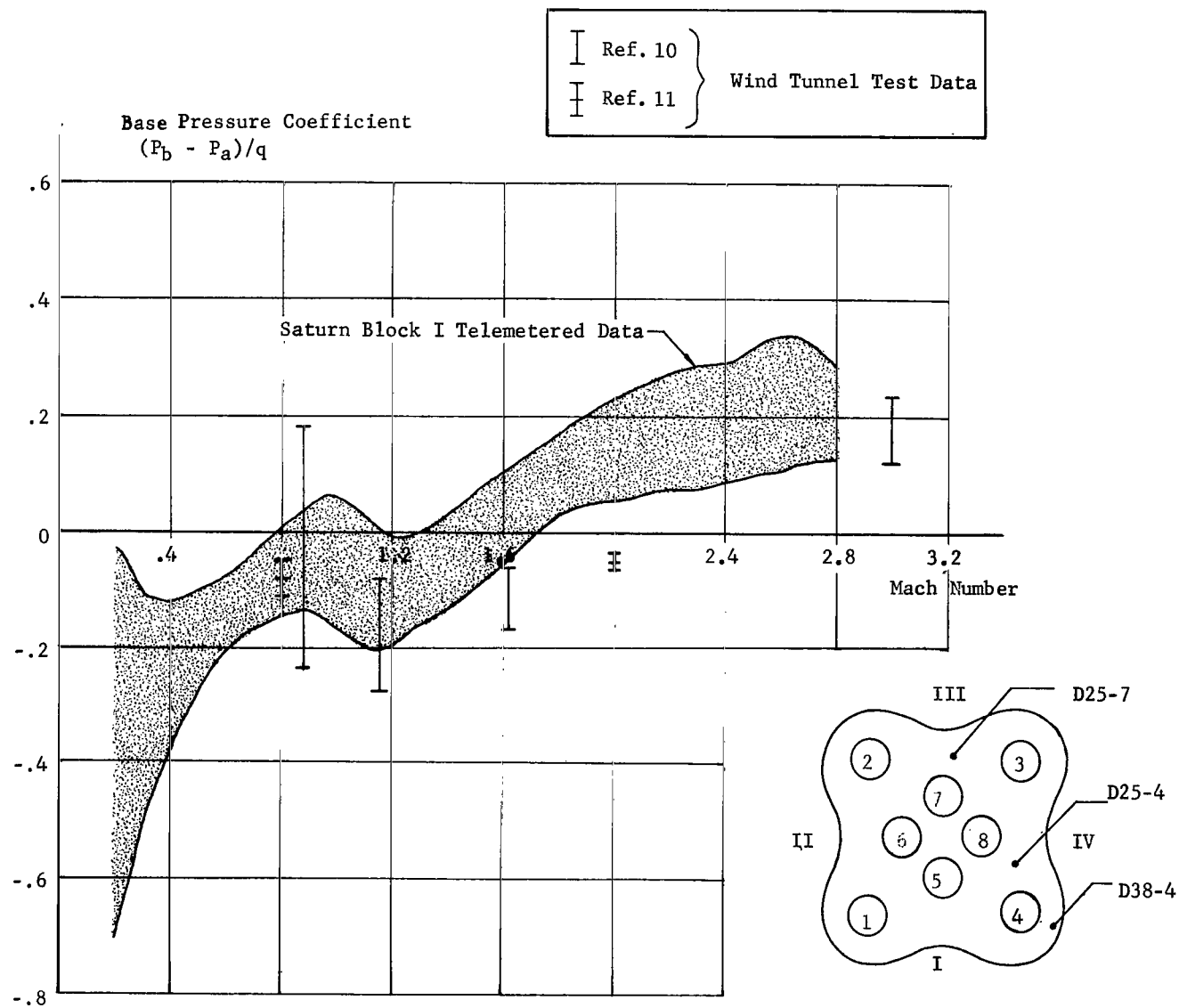
FIGURE 11. BASE PRESSURE COEFFICIENT VERSUS MACH NUMBER
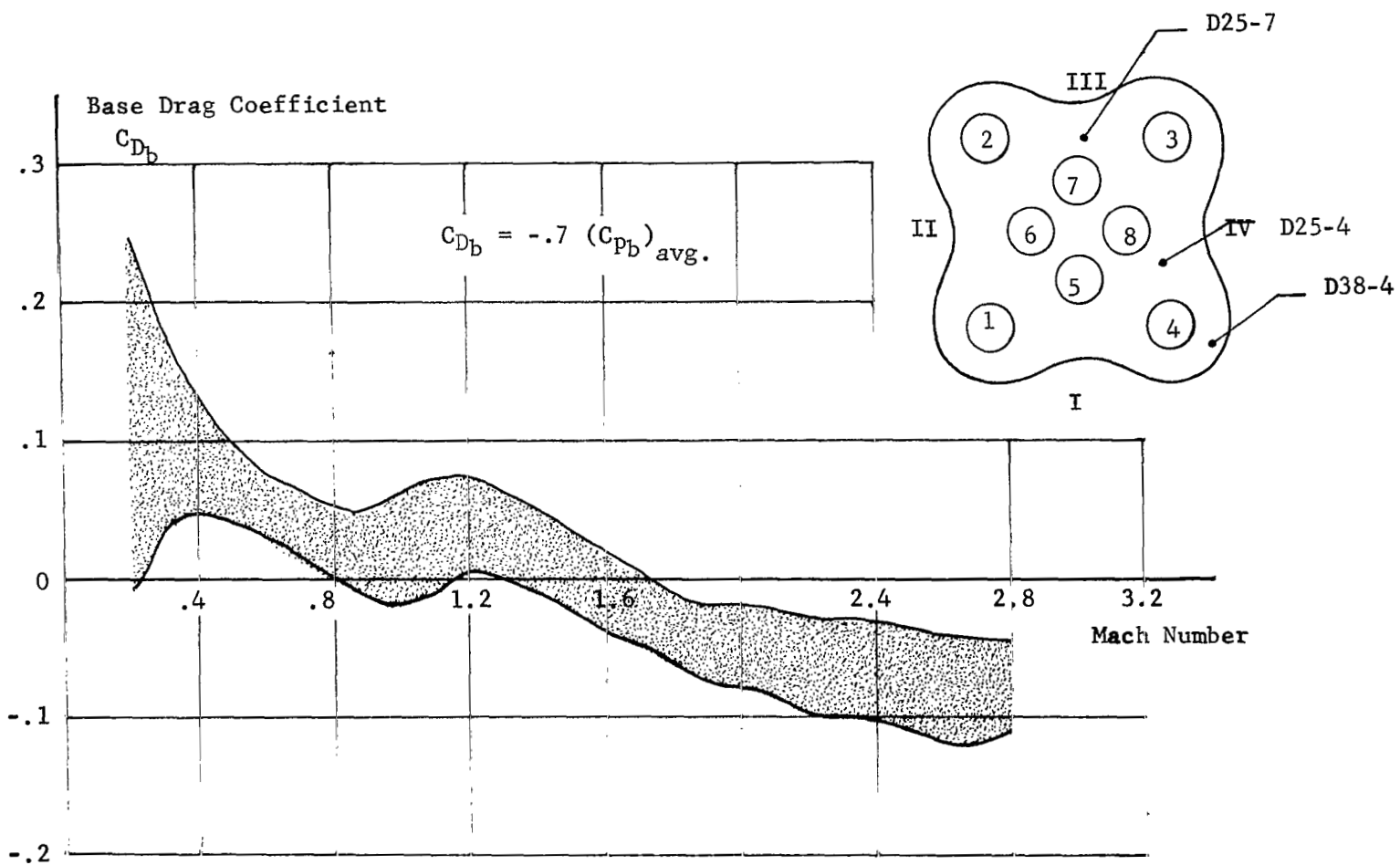
FIGURE 12. BASE DRAG COEFFICIENT VERSUS MACH NUMBER

Pressure Coefficient
$(P - P_a)/q$

.8

.6

.4

.2

0

-.2

-.4

-.6

-.8

.4   .8   1.2   1.6   2.0   2.4   2.8   3.2

Mach   Number

Saturn Block I Telemetered Data

III

D78-10

II   IV

I

D76-10
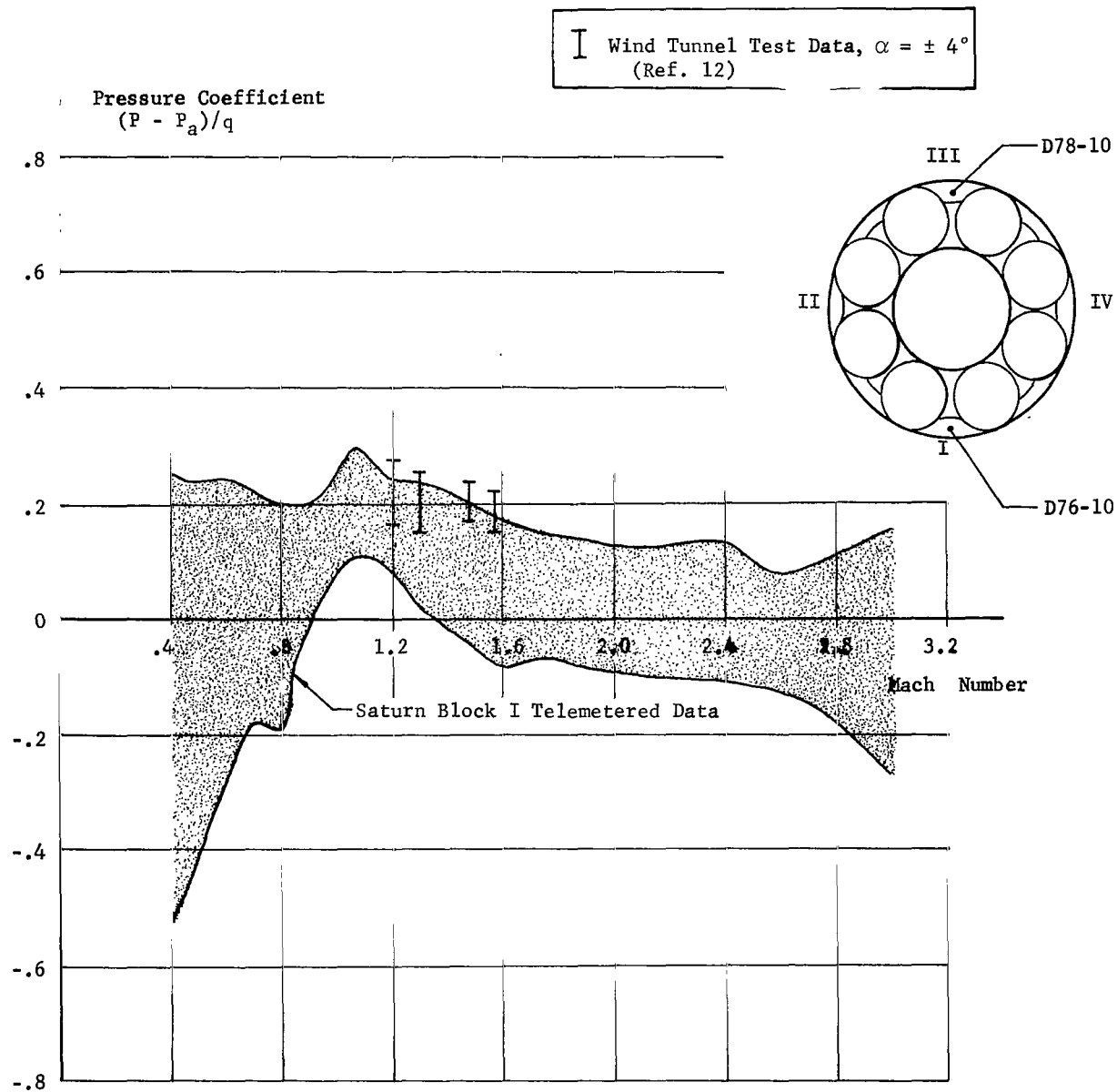
FIGURE 13a.   PRESSURE COEFFICIENT VERSUS MACH NUMBER, FILLETS,
STATION 205
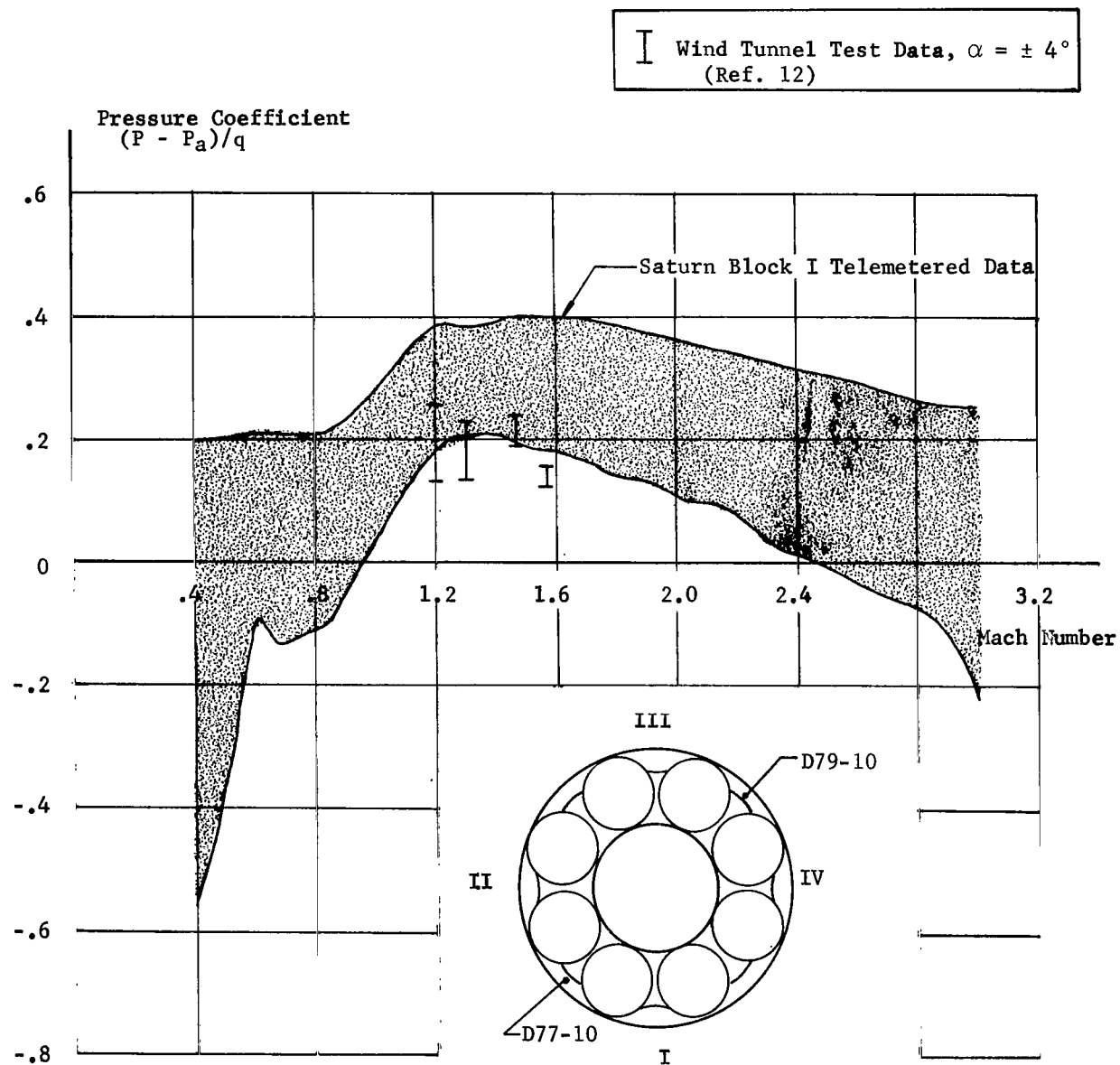
FIGURE 13b. PRESSURE COEFFICIENT VERSUS MACH NUMBER, FILLETS, STATION 205
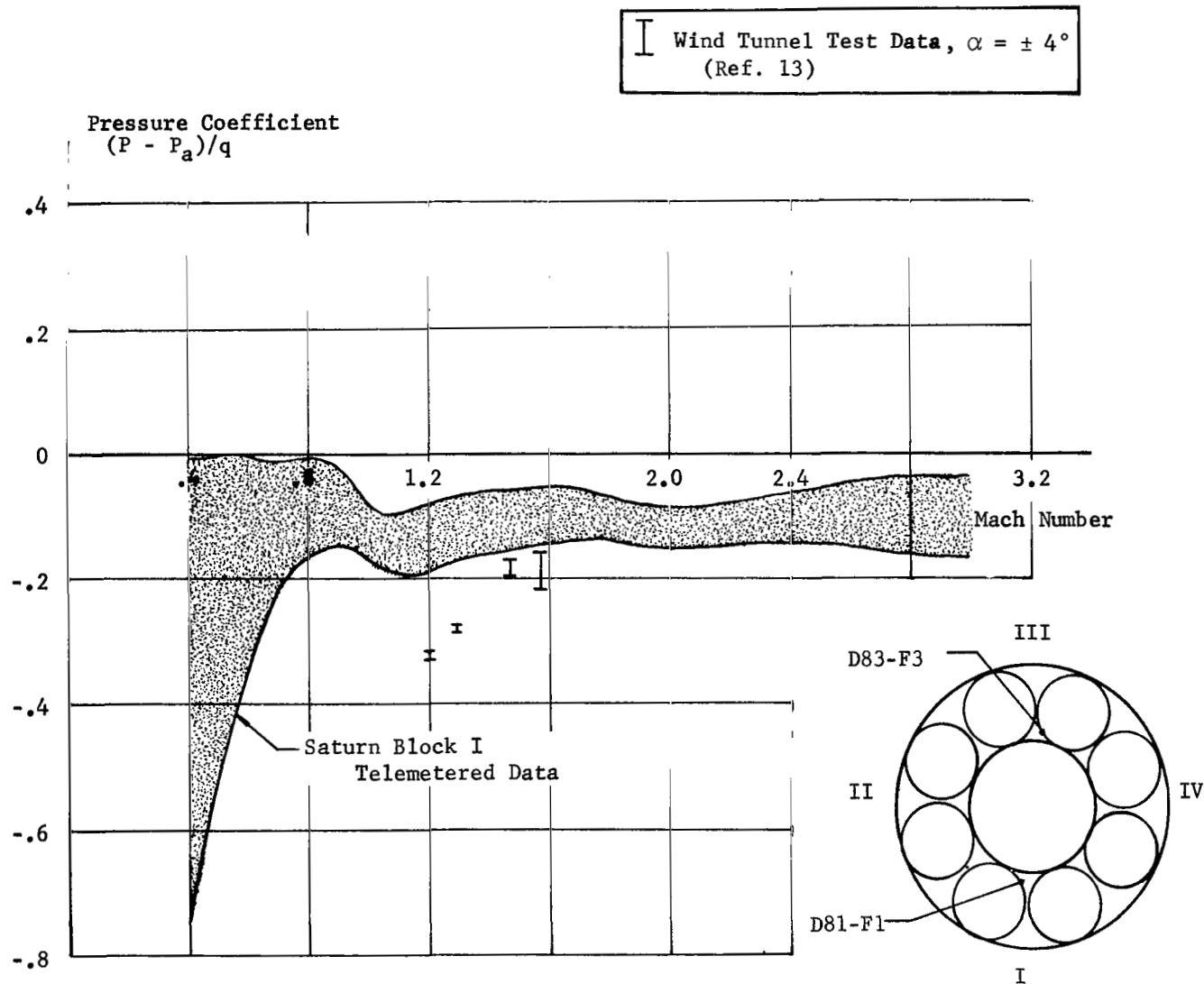
FIGURE 14. PRESSURE COEFFICIENT VERSUS MACH NUMBER, FUEL CONTAINERS, STATION 860
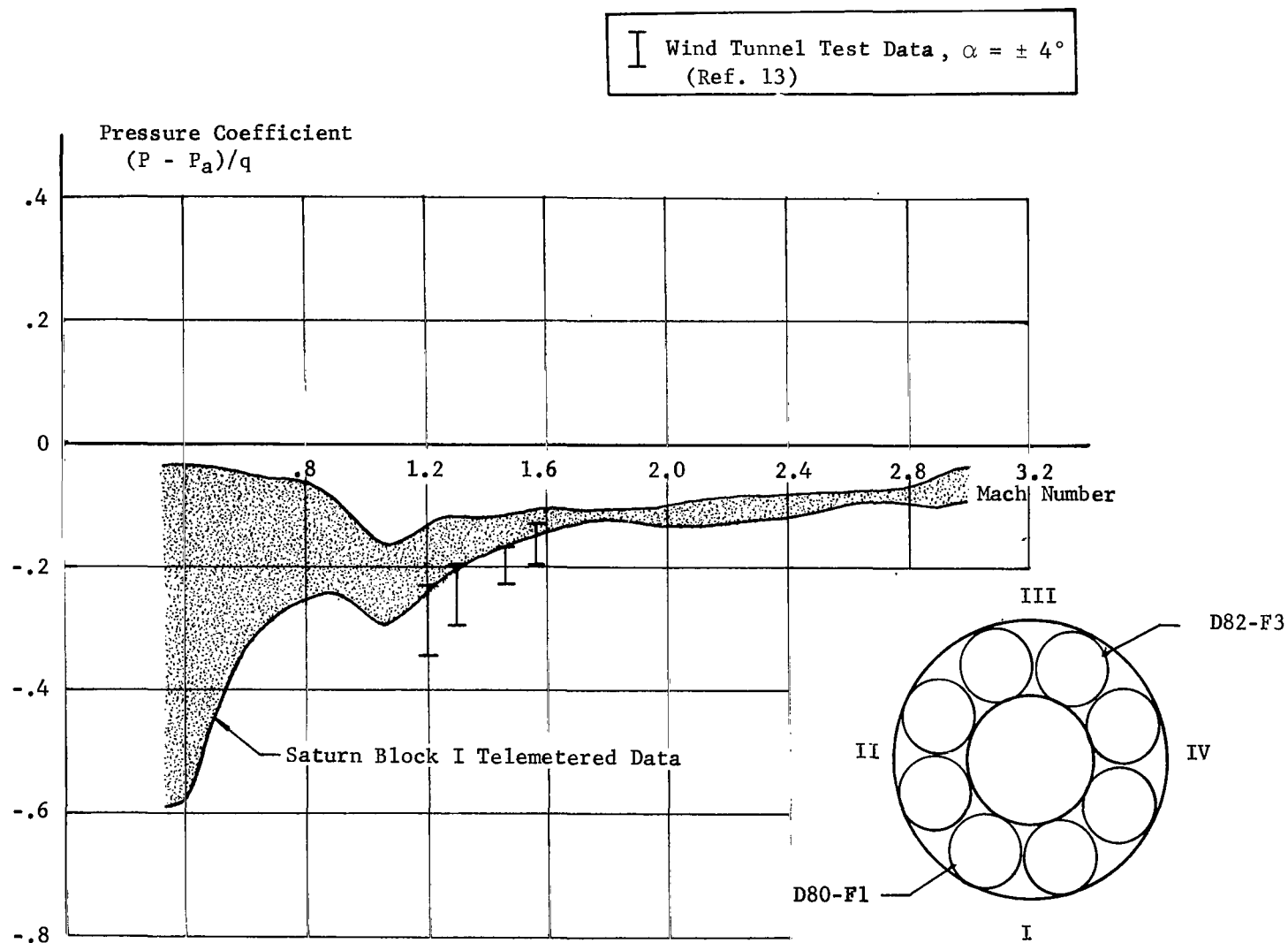
FIGURE 15. PRESSURE COEFFICIENT VERSUS MACH NUMBER, FUEL CONTAINERS, STATION 863
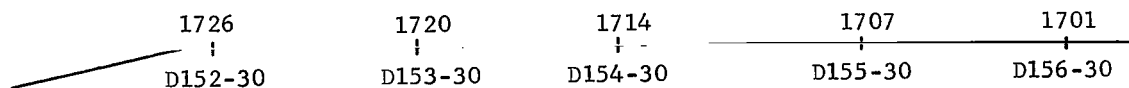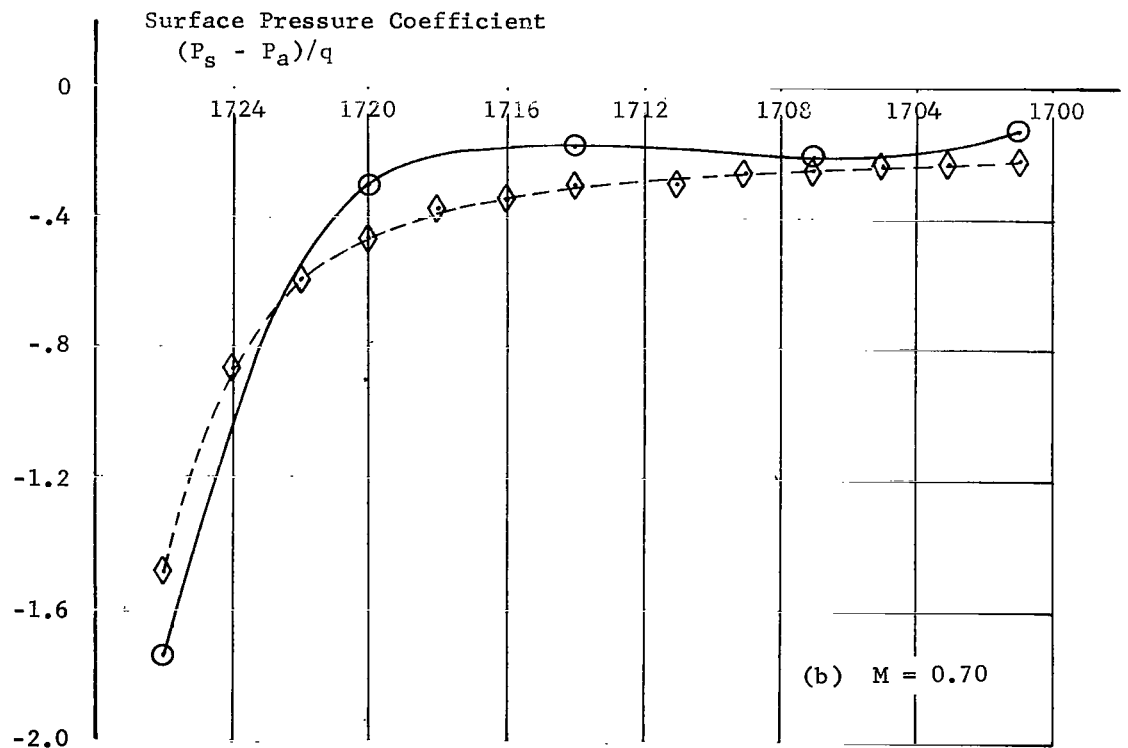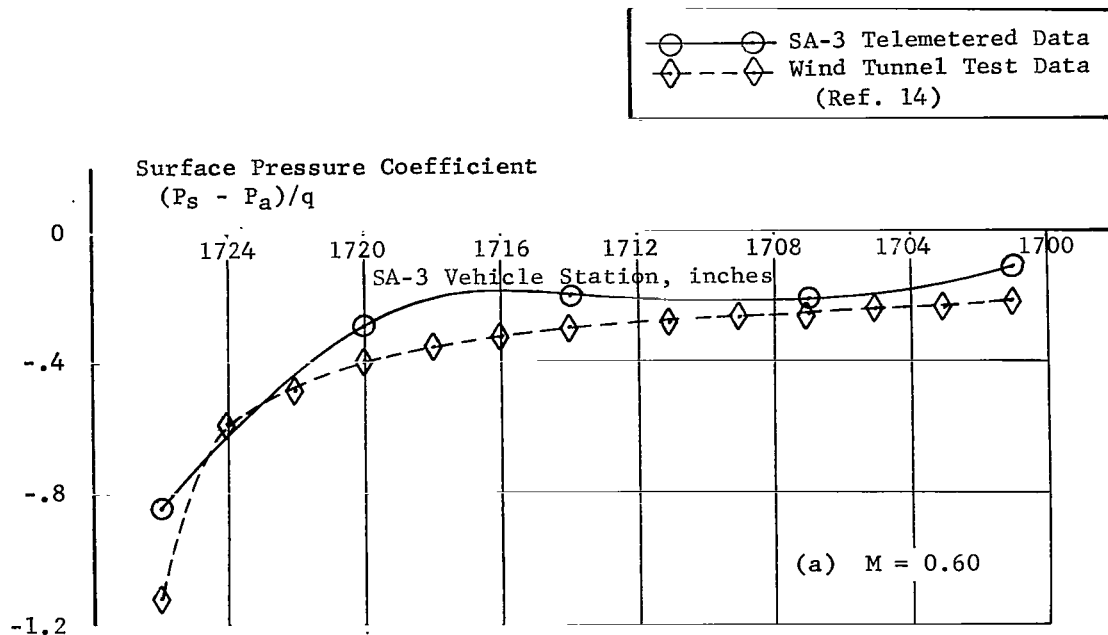
FIGURE 16(a,b). SURFACE PRESSURE COEFFICIENT VERSUS LONGITUDINAL
STATION, SA-3 DUMMY PAYLOAD
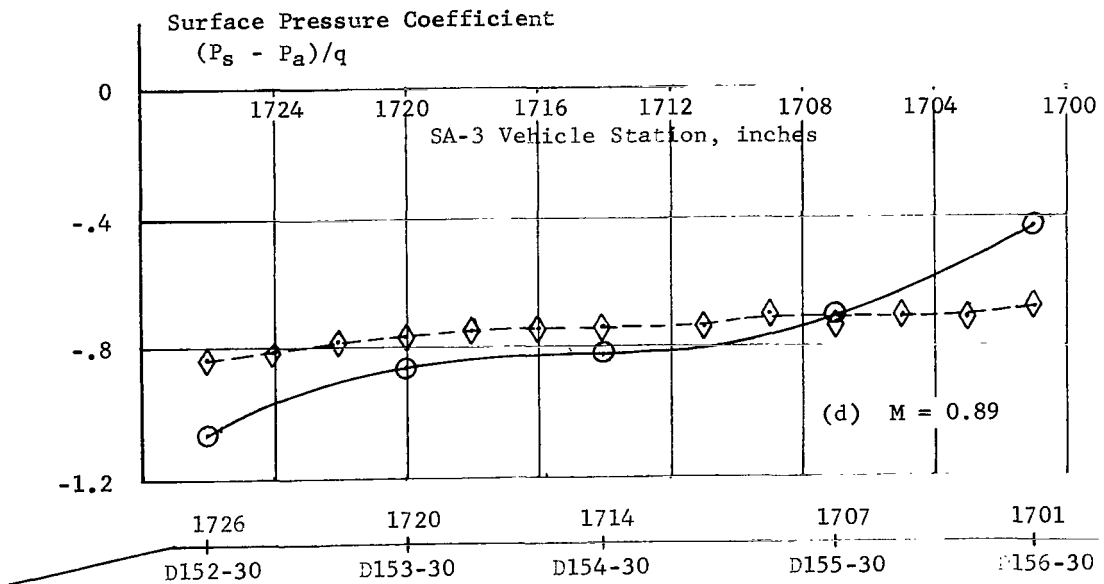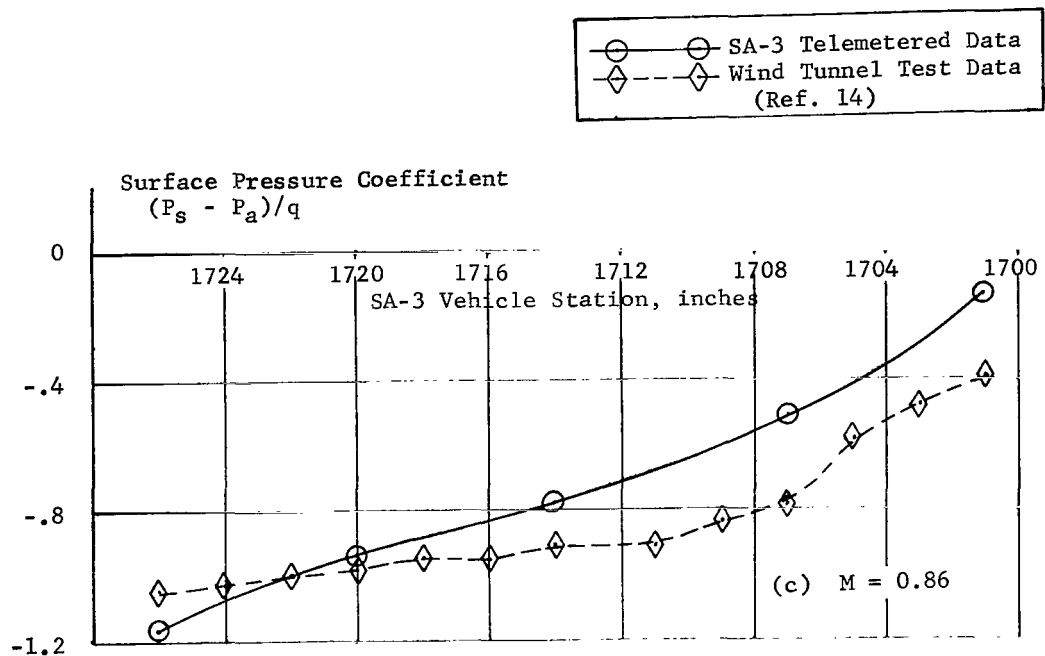
FIGURE 16(c,d). SURFACE PRESSURE COEFFICIENT VERSUS LONGITUDINAL
STATION, SA-3 DUMMY PAYLOAD
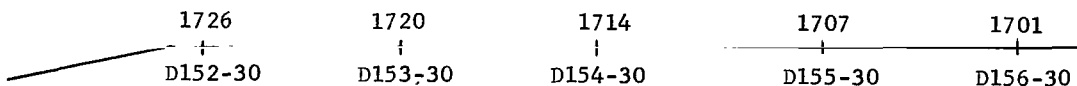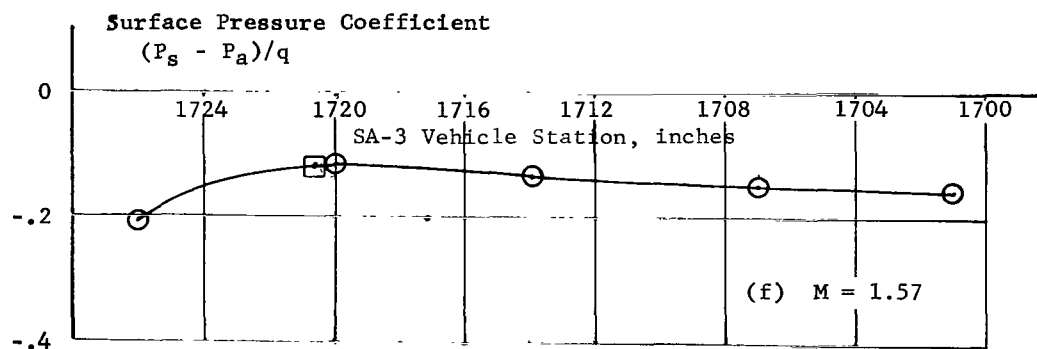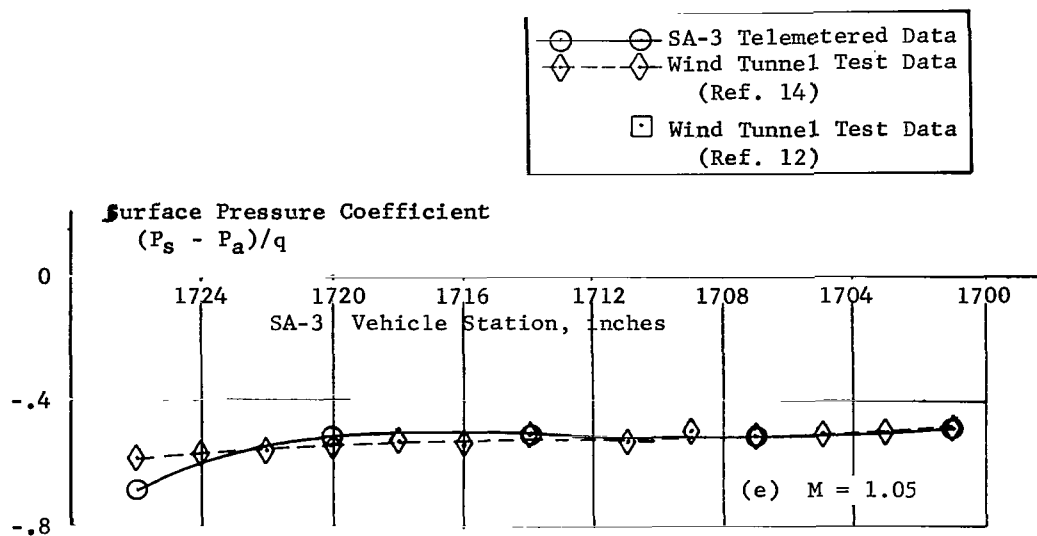
FIGURE 16(e,f). SURFACE PRESSURE COEFFICIENT VERSUS LONGITUDINAL
STATION, SA-3 DUMMY PAYLOAD

37
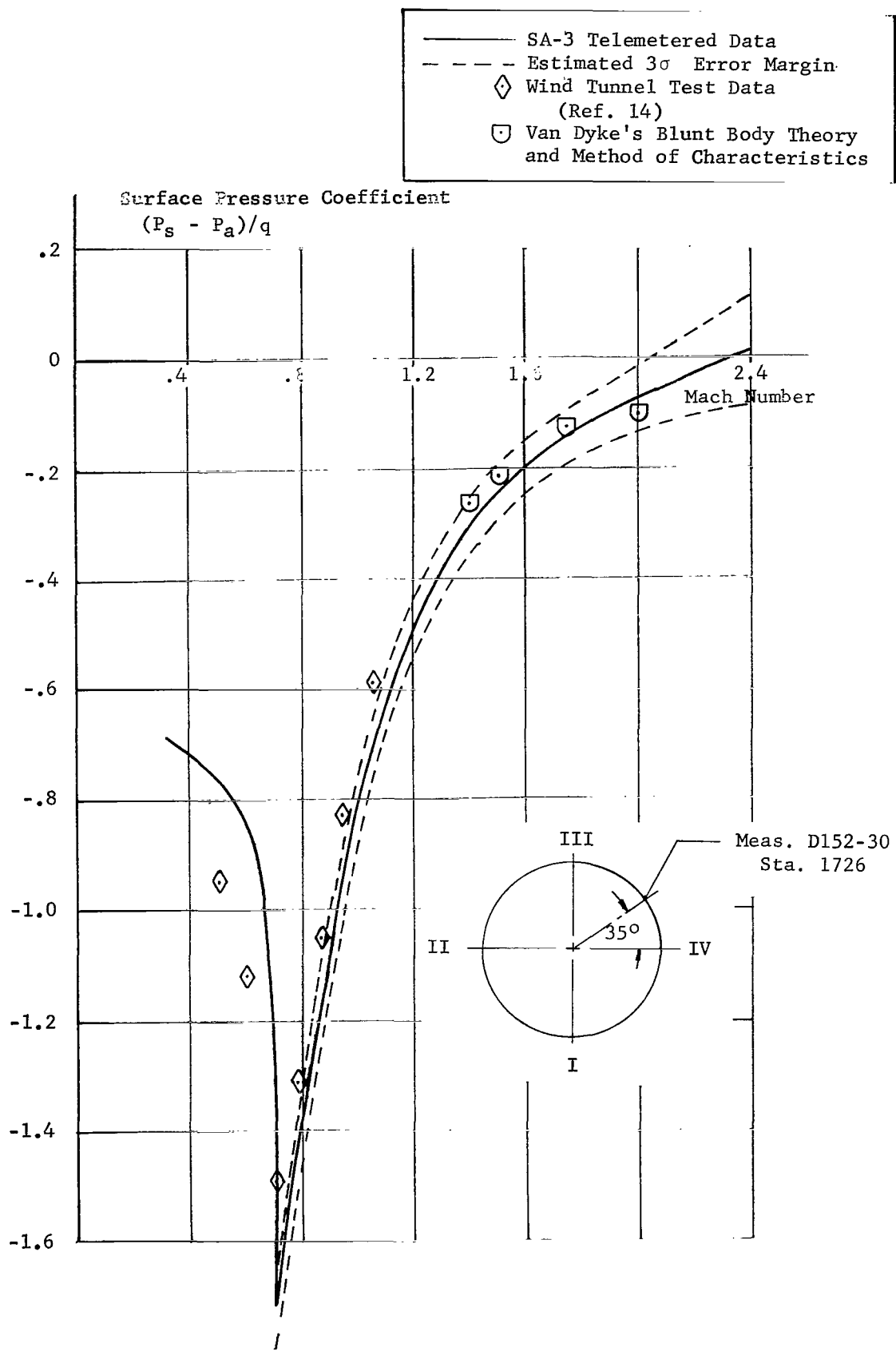
FIGURE 17a. SURFACE PRESSURE COEFFICIENT VERSUS MACH NUMBER, STATION 1726 (SA-3)
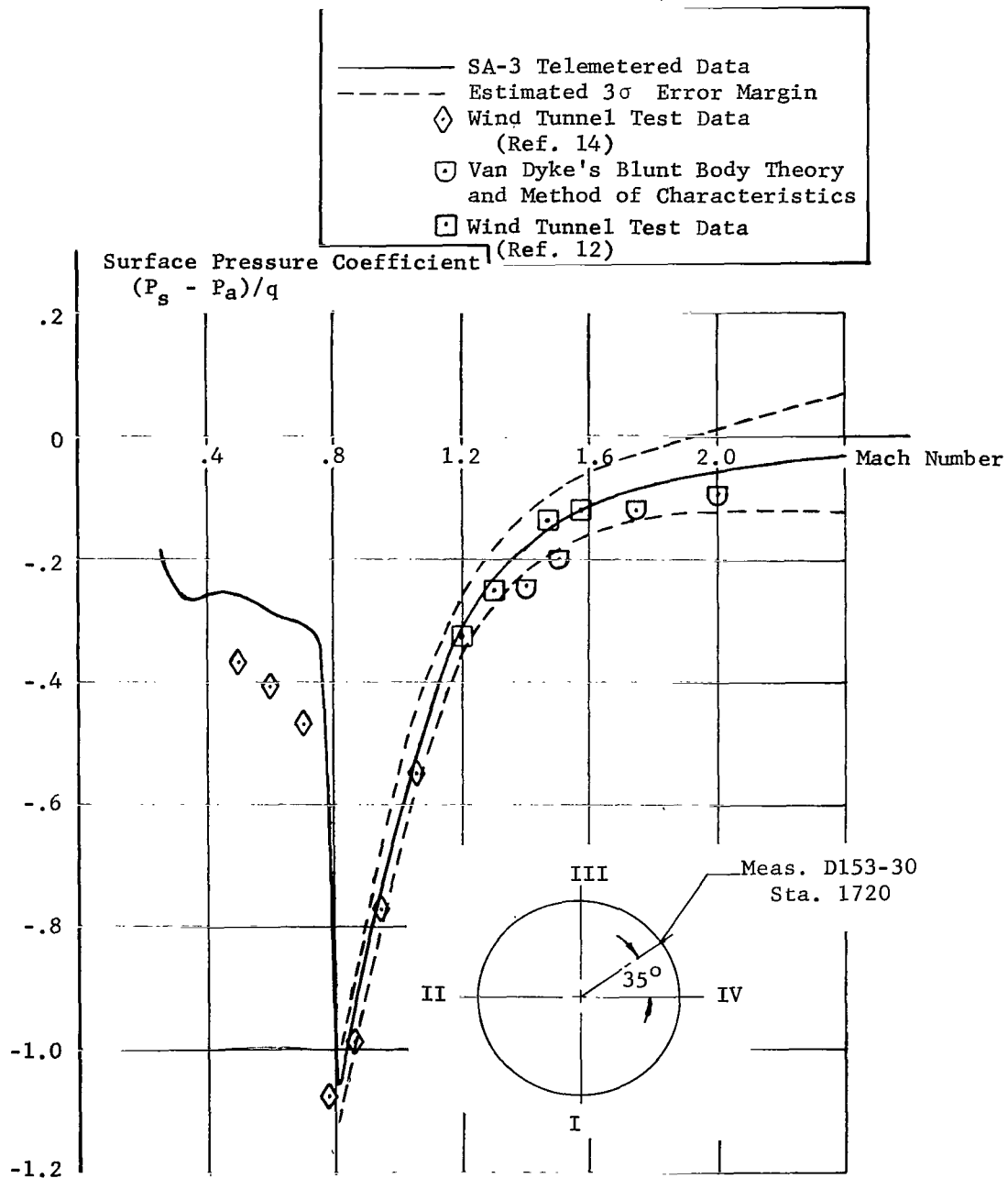
FIGURE 17b. SURFACE PRESSURE COEFFICIENT VERSUS MACH NUMBER, STATION 1720 (SA-3)
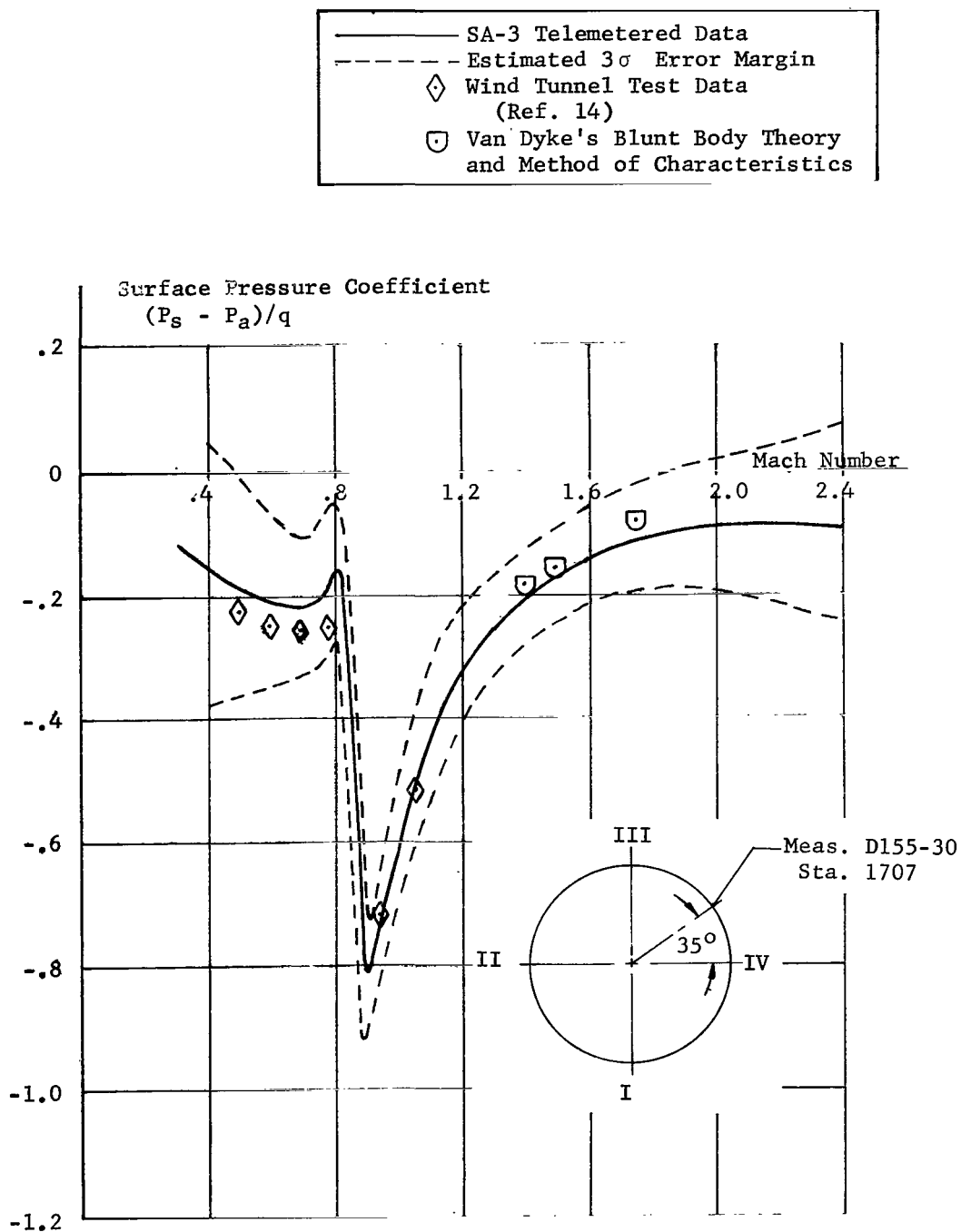
FIGURE 17c. SURFACE PRESSURE COEFFICIENT VERSUS MACH NUMBER,
STATION 1707 (SA-3)
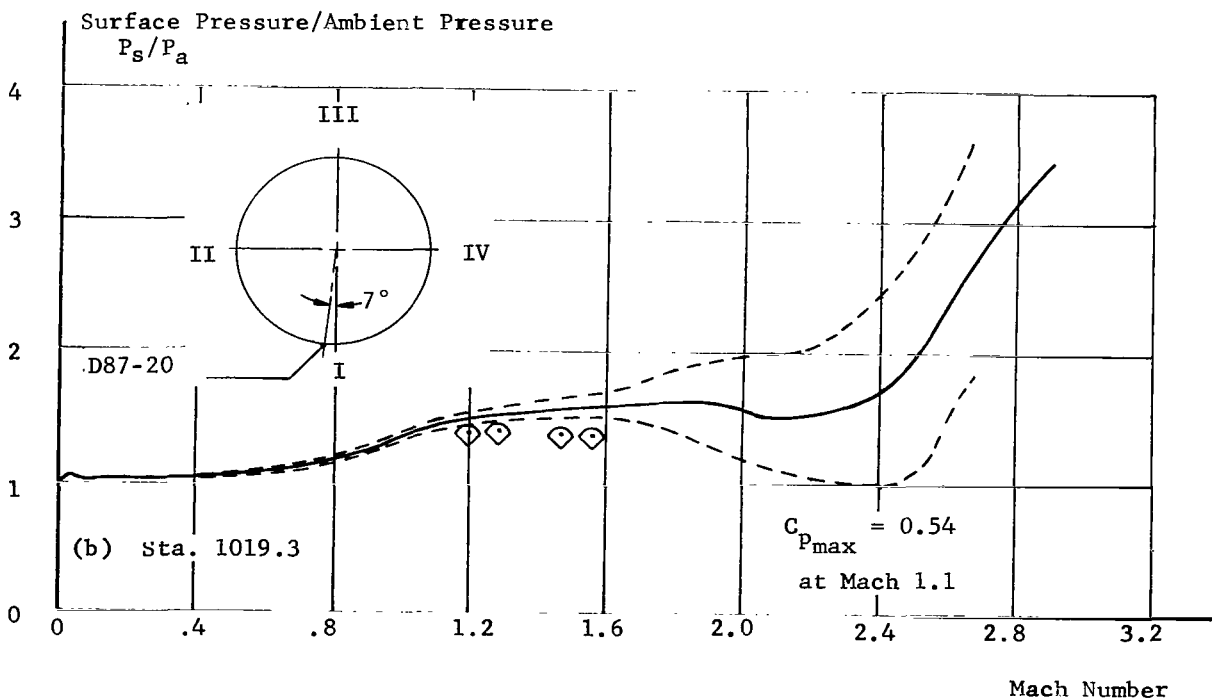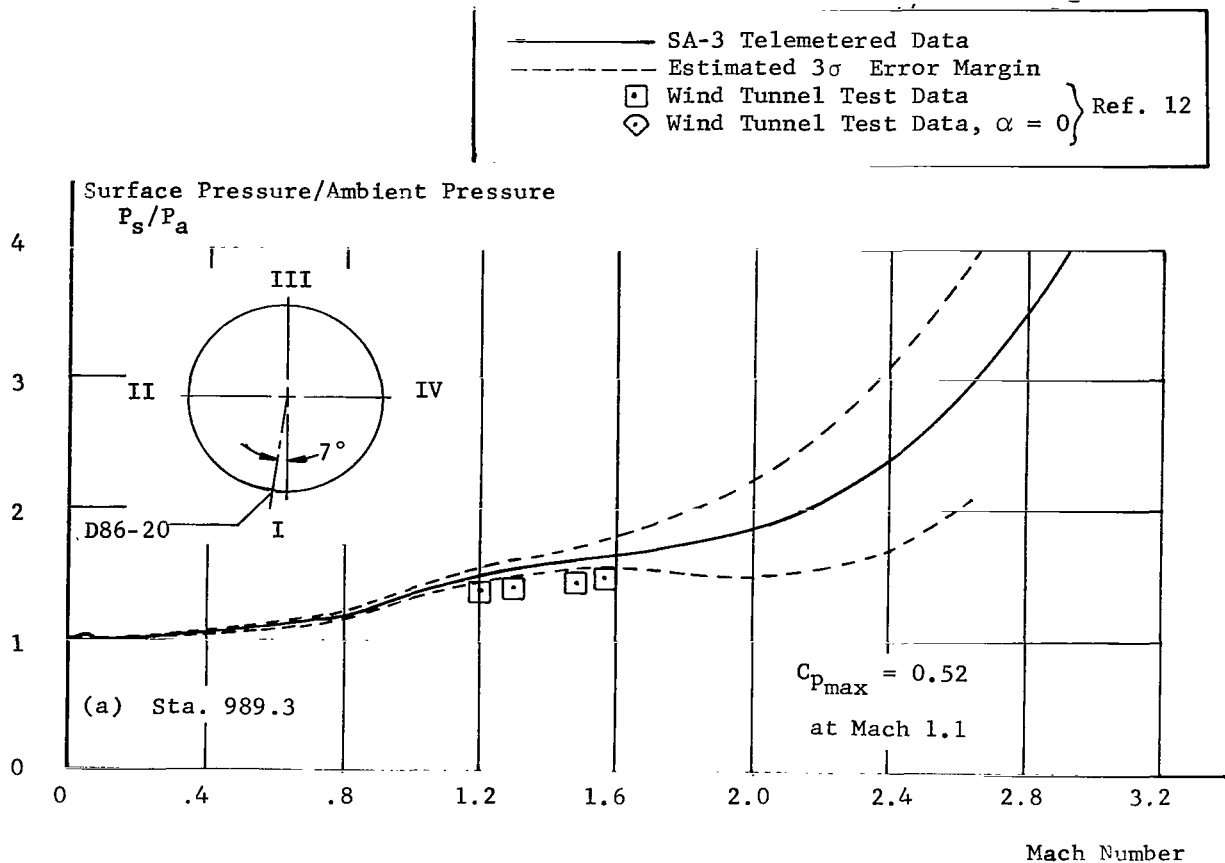
FIGURE 18(a,b). RATIO OF SURFACE PRESSURE TO AMBIENT PRESSURE
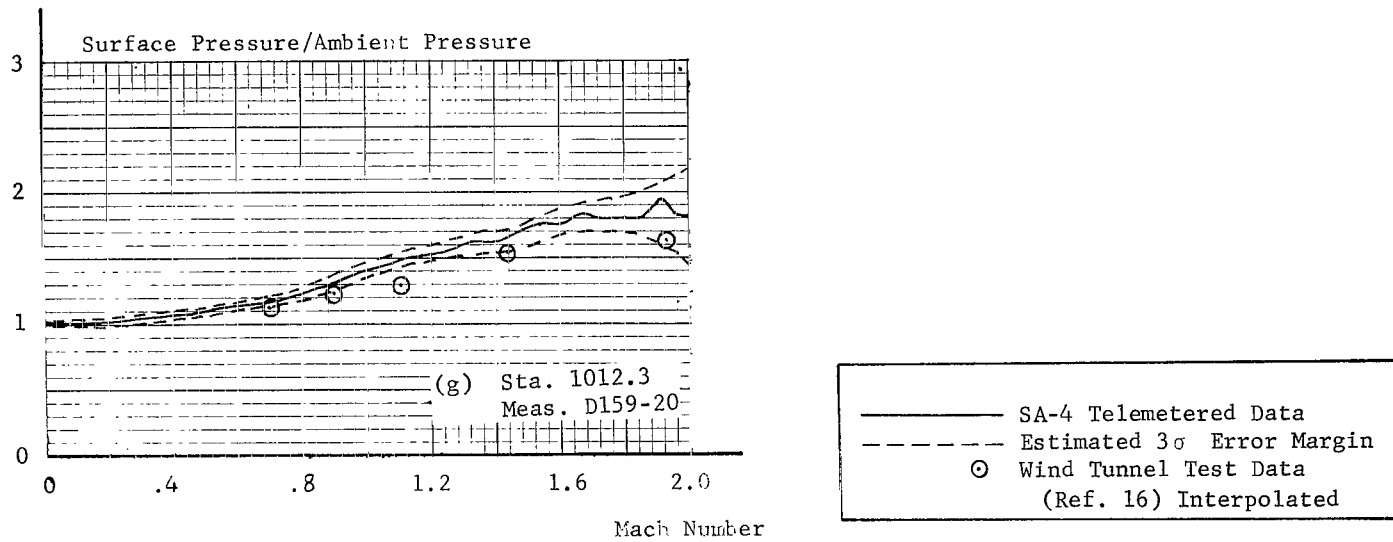   VERSUS MACH NUMBER, LEEWARD SIDE, SA-3   41
                INTERSTAGE

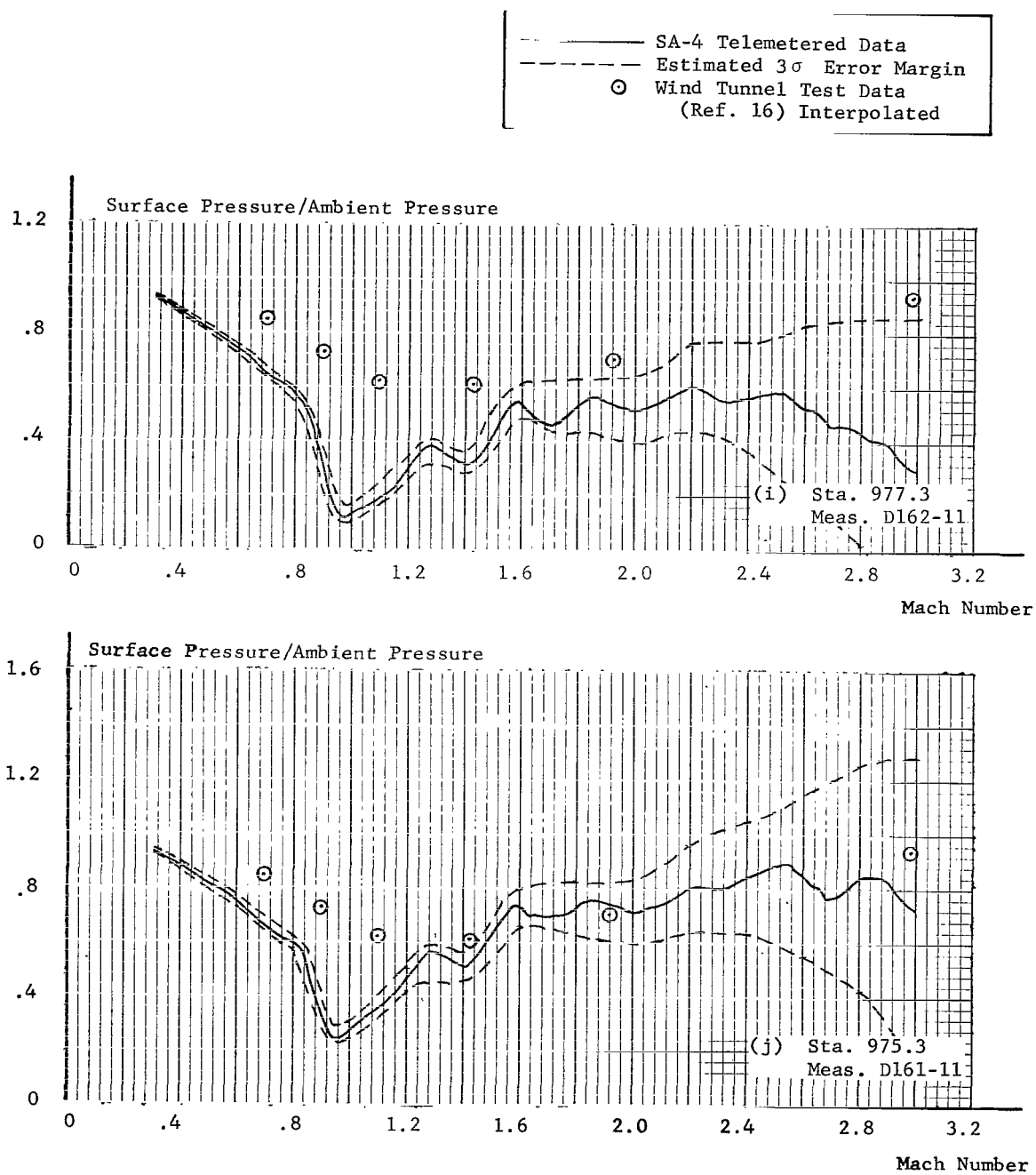FIGURE 19(a,b). RATIO OF SURFACE PRESSURE TO AMBIENT PRESSURE VERSUS MACH NUMBER, WINDWARD SIDE, SA-3 INTERSTAGE

42

● Absolute Pressure Measurements
+ Sound Intensity AC Amplifier
  Piezoelectric Microphone
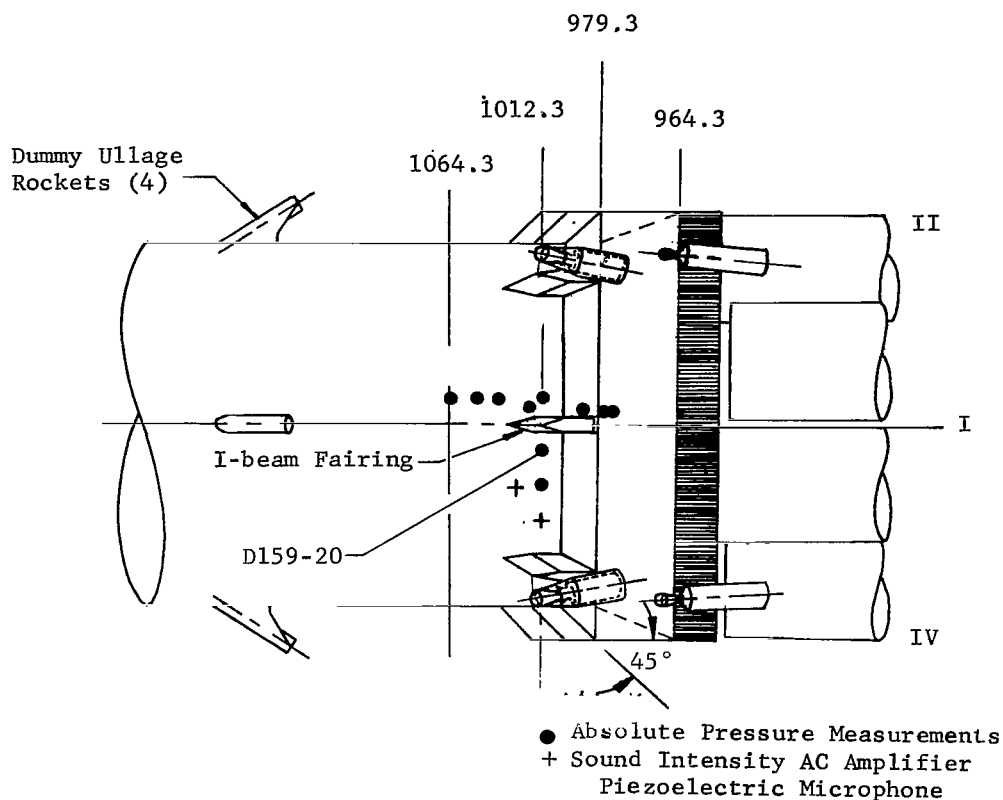
Station (inches)	Meas. No.	Φ * (deg)	Range	Manufacturer	Type	Model	Response+ (cps)
1064.3	D167-20	8	0-25 psia	Servonics	Potentiometer	L127-3	C
1049.3	D166-20	8	0-25 psia	Servonics	Potentiometer	L127-3	C
1038.3	D165-20	8	0-25 psia	Servonics	Potentiometer	L127-3	C
1029.3	L65-20	-22	145-165 db	Gulton	Microphone	P420M-6	Over 500
1019.3	D87-20	7	0-25 psia	Servonics	Potentiometer	L127-3	25
1012.3	D164-20	8	0-15 psia	Servonics	Potentiometer	L158-2	C
1012.3	D159-20	-8	0-15 psia	Statham	Strain Gauge	PA203	330
1012.3	D160-20	-20	0-15 psia	Servonics	Potentiometer	L158-2	25
1012.3	L64-20	-33	145-165 db	Gulton	Microphone	P420M-6	Over 500
989.3	D163-20	4	0-15 psia	Statham	Strain Gauge	PA203	45
977.3	D162-11	4	0-15 psia	Servonics	Potentiometer	L158-2	C
975.3	D161-11	4	0-15 psia	Servonics	Potentiometer	L158-2	C

* Angle measured positive from I to II
C - Commutated channel, 10 samples/sec, 2.4 cps maximum telemetry response
+ Instrument or telemetry channel, whichever is lower

FIGURE 20. SA-4 INTERSTAGE PRESSURE MEASUREMENTS
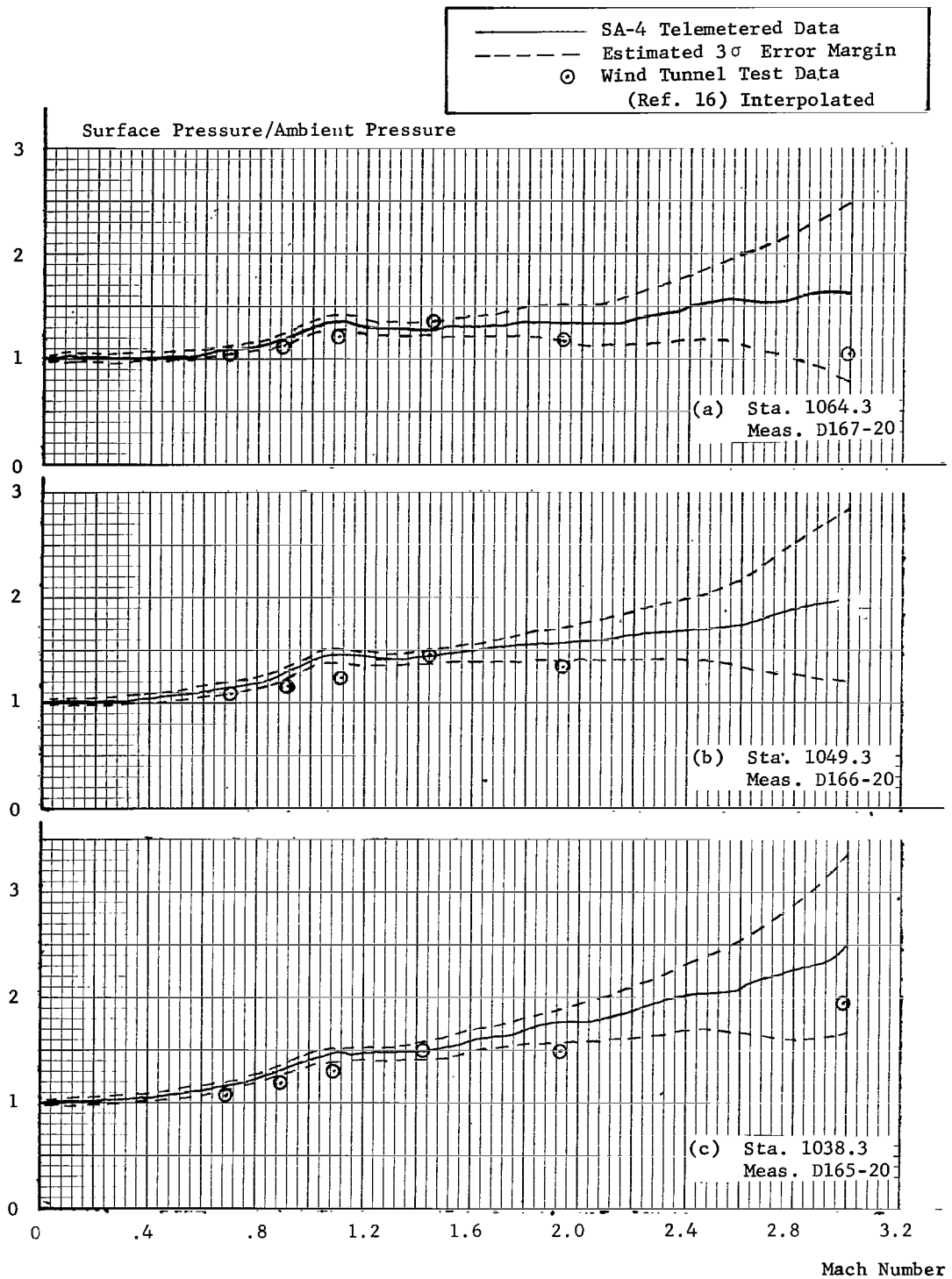
FIGURE 21(a-c). RATIO OF SURFACE PRESSURE TO AMBIENT PRESSURE
VERSUS MACH NUMBER, SA-4 INTERSTAGE
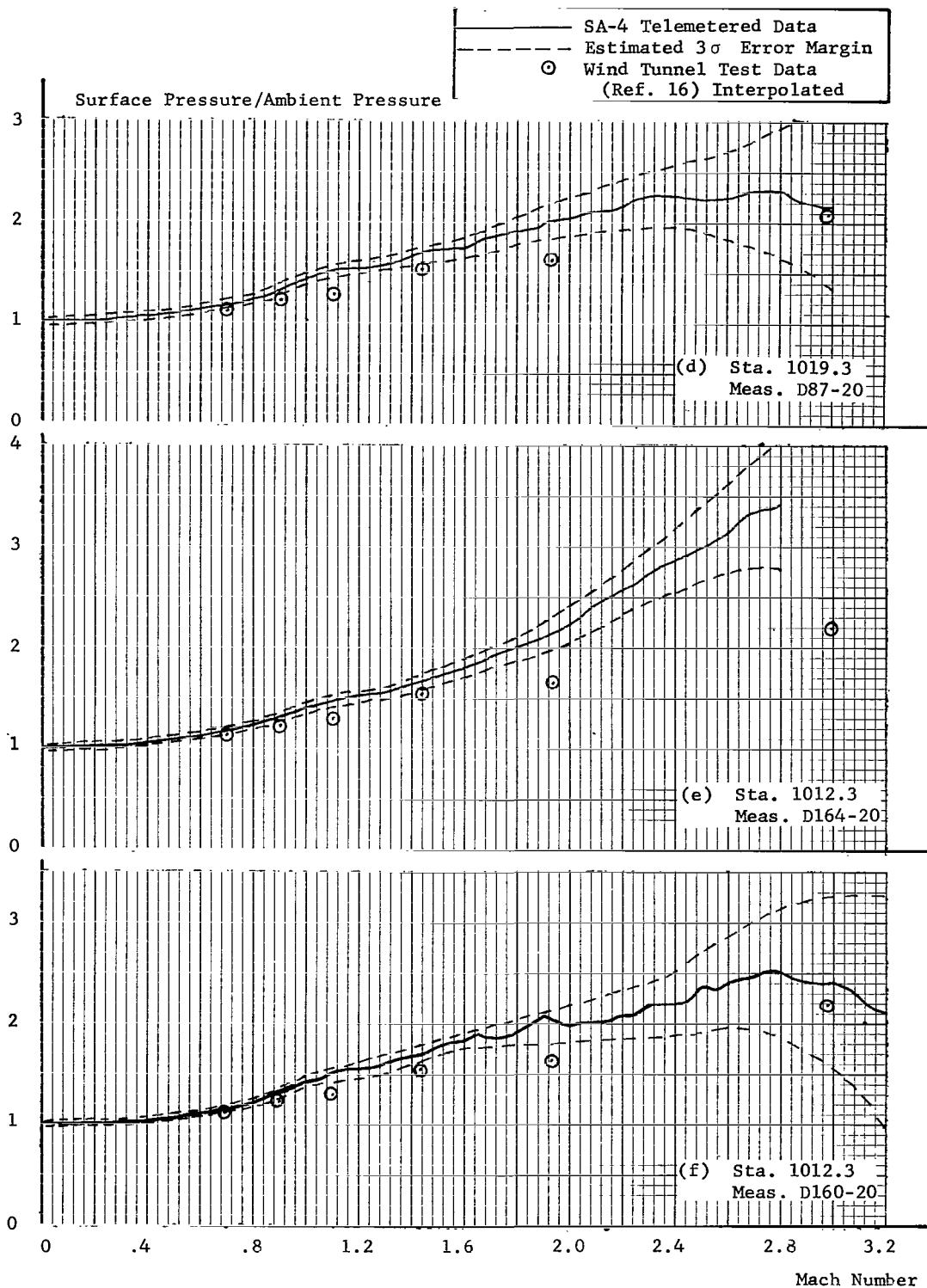
FIGURE 21(d-f). RATIO OF SURFACE PRESSURE TO AMBIENT PRESSURE
VERSUS MACH NUMBER, SA-4 INTERSTAGE
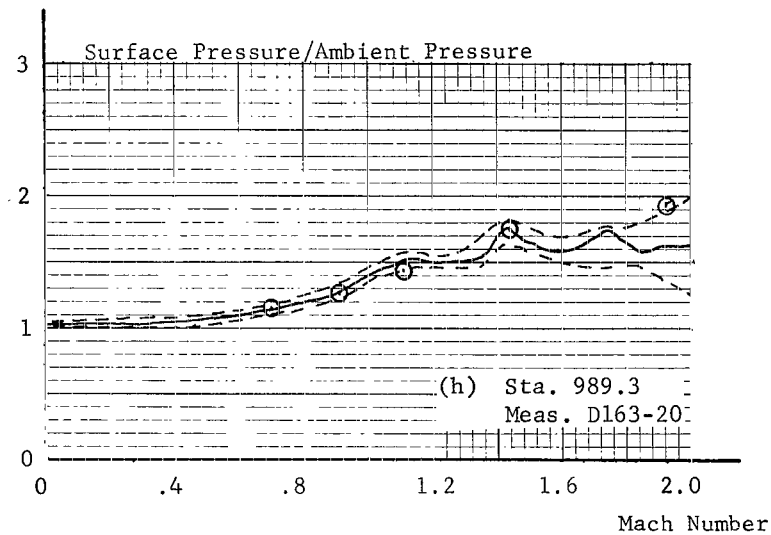
FIGURE 21(g,h). RATIO OF SURFACE PRESSURE TO AMBIENT PRESSURE VERSUS
MACH NUMBER, SA-4 INTERSTAGE

FIGURE 21(i,j). RATIO OF SURFACE PRESSURE TO AMBIENT PRESSURE VERSUS MACH NUMBER, SA-4 INTERSTAGE
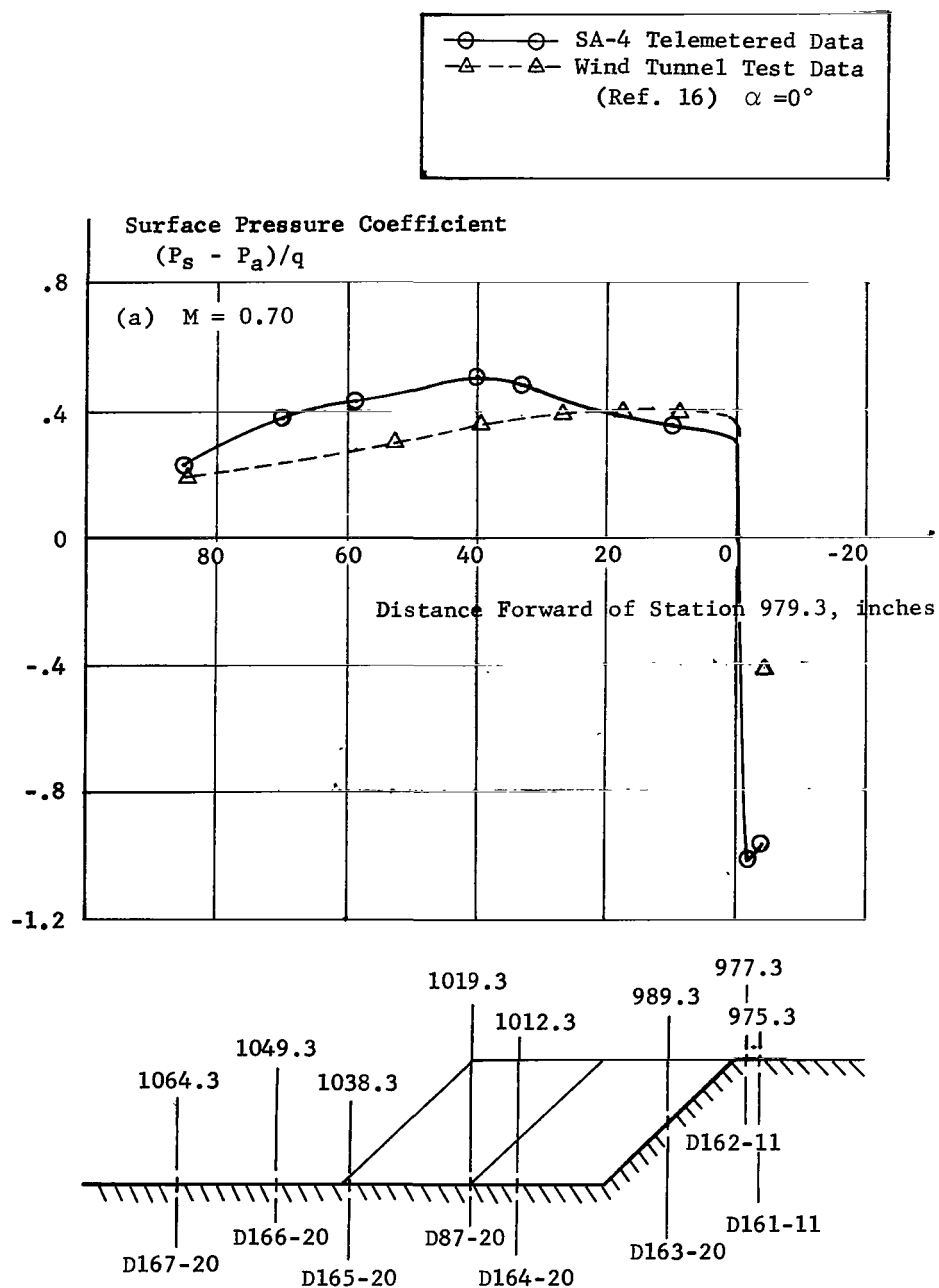
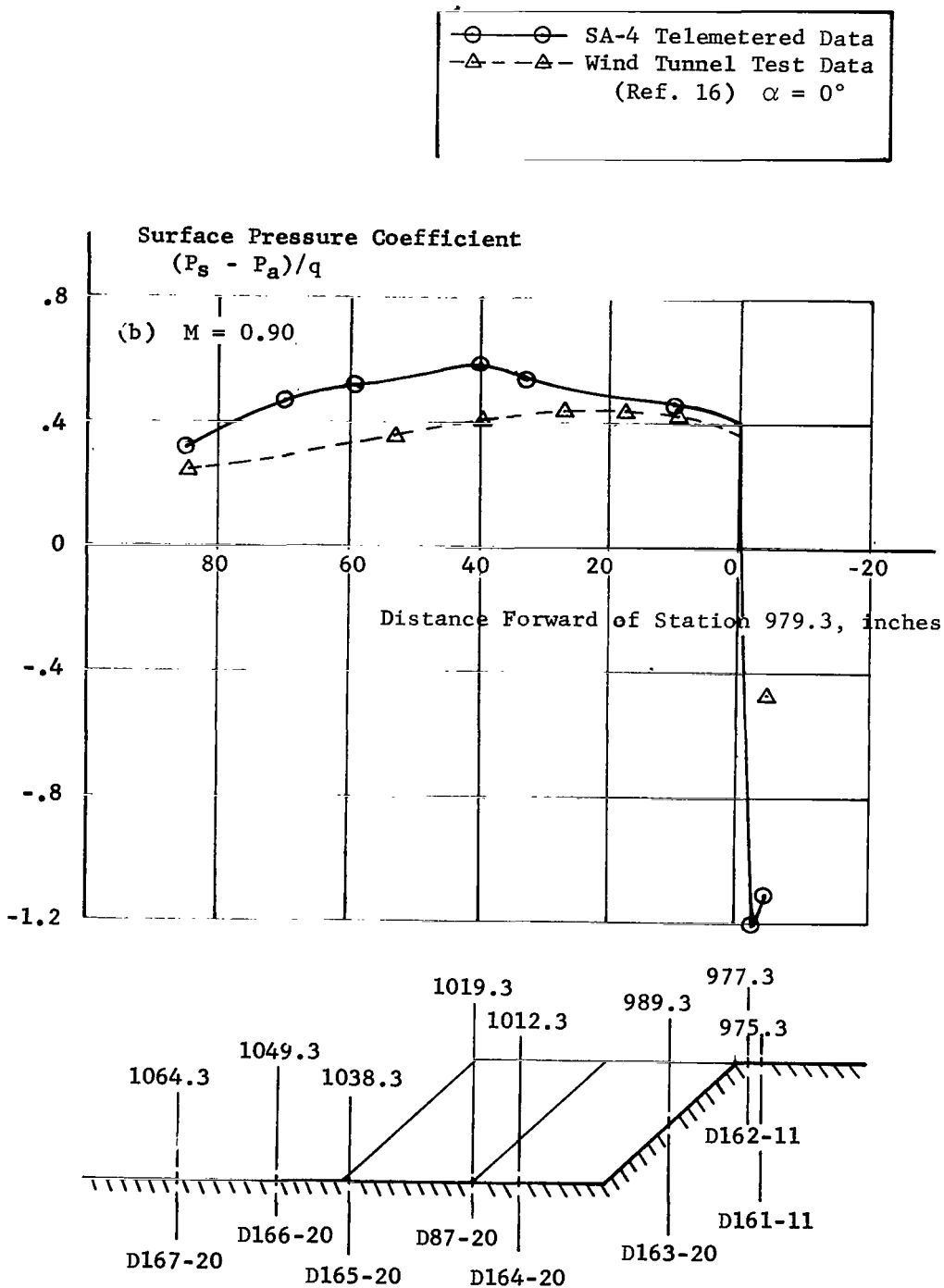FIGURE 22a. SURFACE PRESSURE COEFFICIENT VERSUS LONGITUDINAL STATION, SA-4 INTERSTAGE

FIGURE 22b. SURFACE PRESSURE COEFFICIENT VERSUS LONGITUDINAL STATION, SA-4 INTERSTAGE
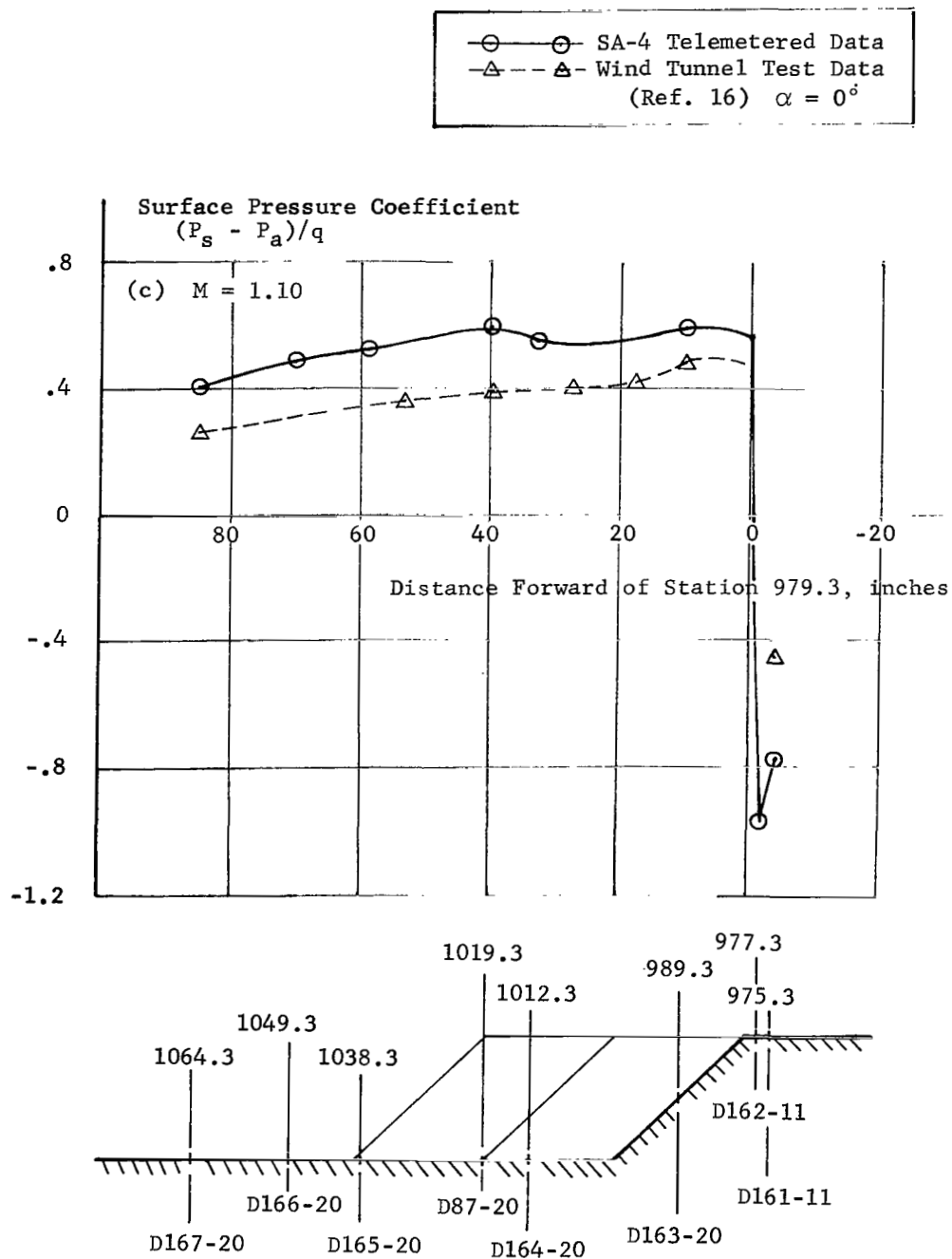
FIGURE 22c. SURFACE PRESSURE COEFFICIENT VERSUS LONGITUDINAL STATION, SA-4 INTERSTAGE
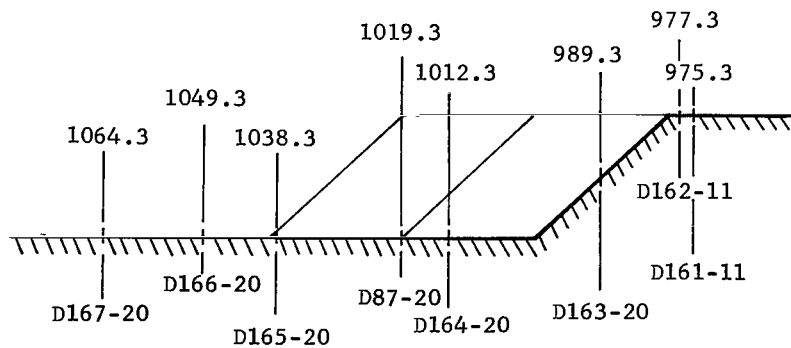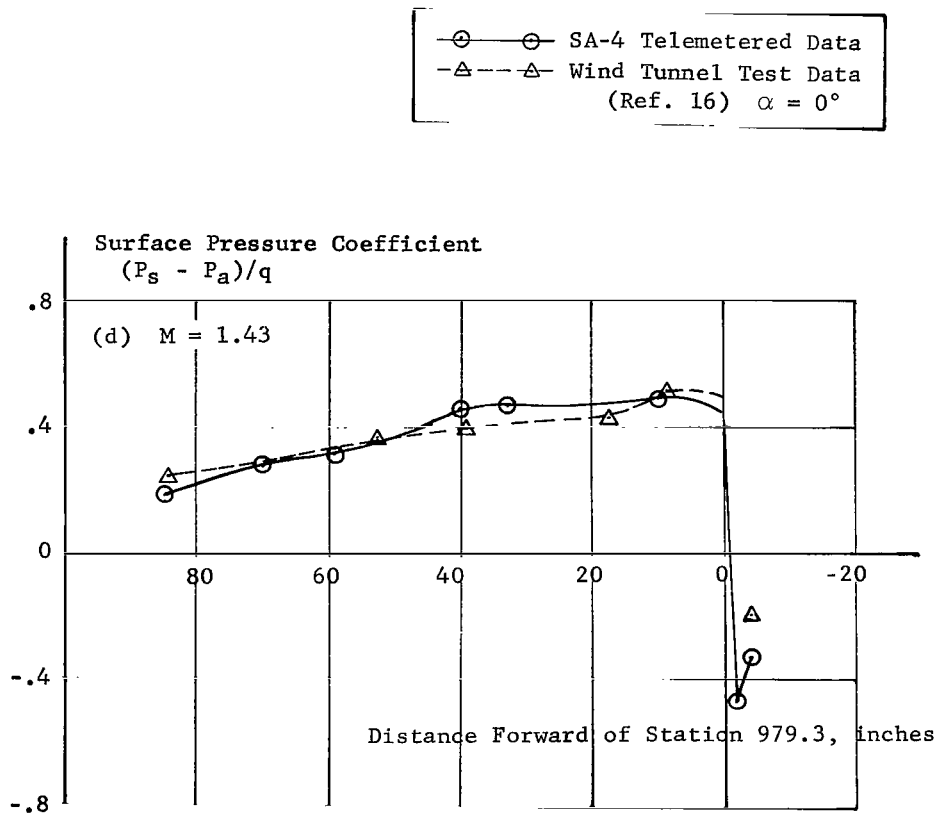
FIGURE 22d. SURFACE PRESSURE COEFFICIENT VERSUS LONGITUDINAL STATION, SA-4 INTERSTAGE
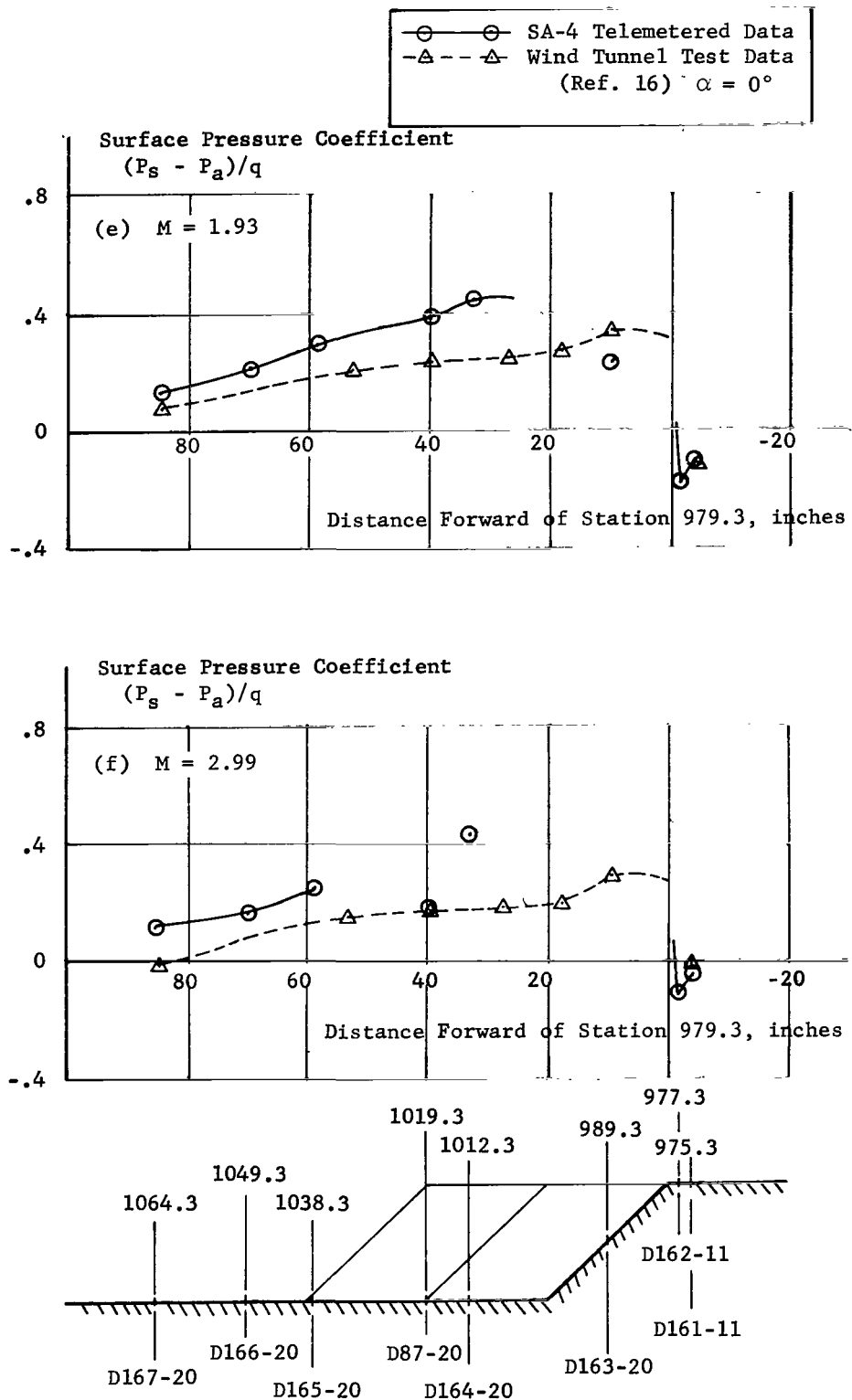
FIGURE 22(e,f). SURFACE PRESSURE COEFFICIENT VERSUS LONGITUDINAL
STATION SA-4 INTERSTAGE
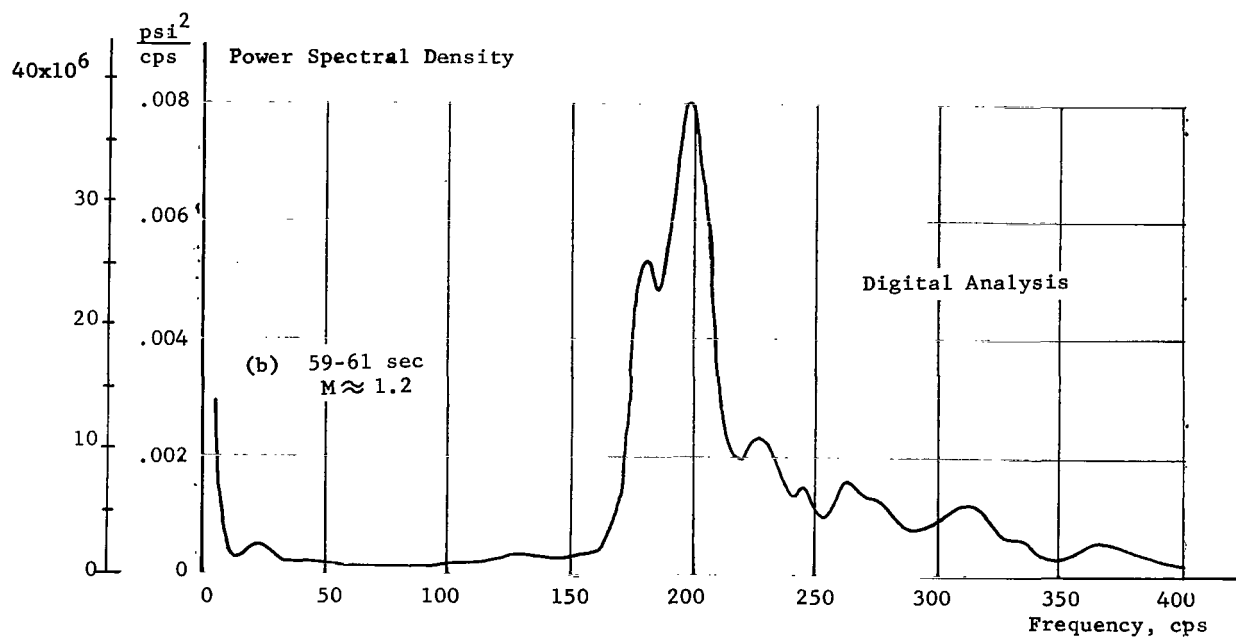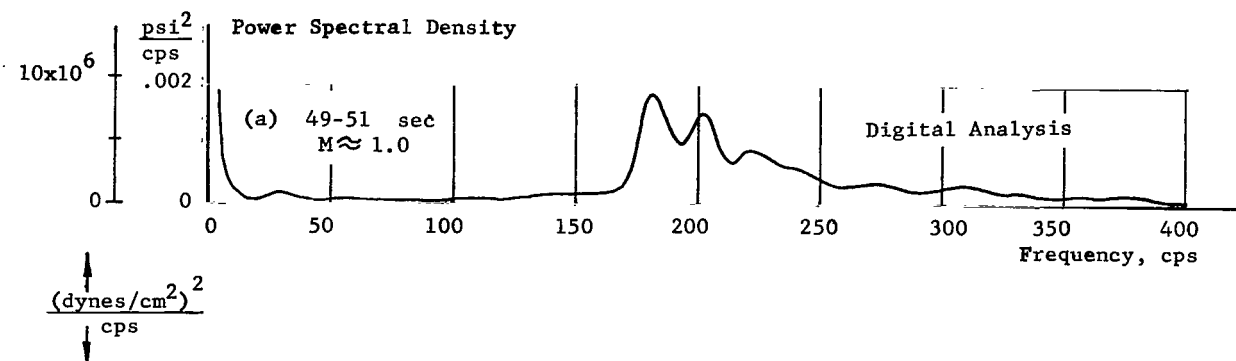
FIGURE 23(a,b). POWER SPECTRAL DENSITIES OF PRESSURE FLUCTUATIONS, MEASUREMENT D159-20
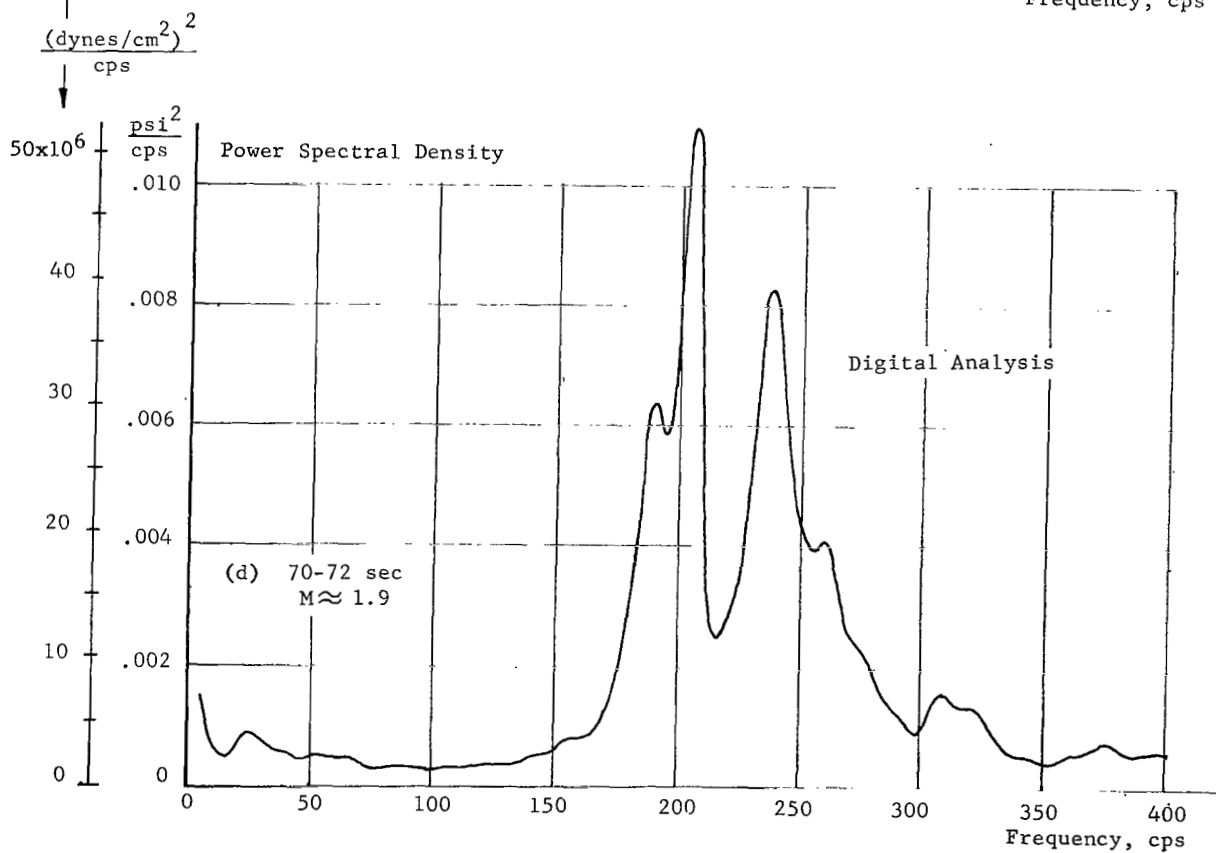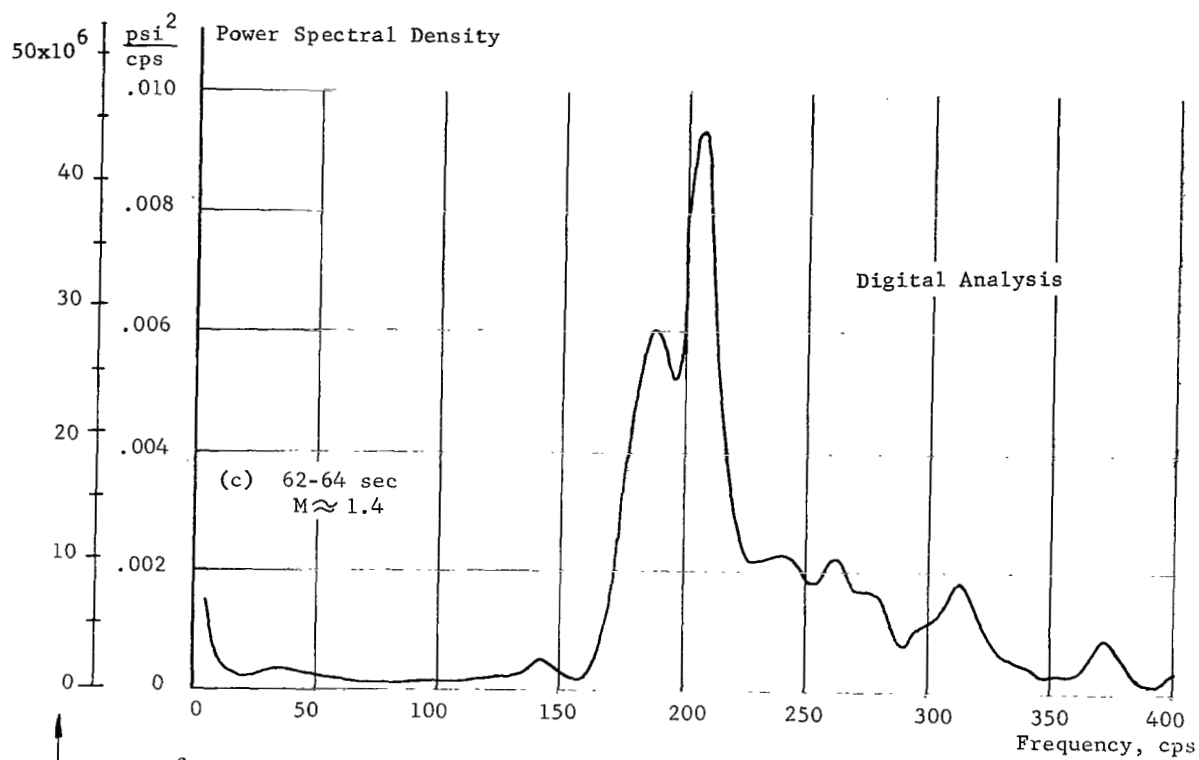
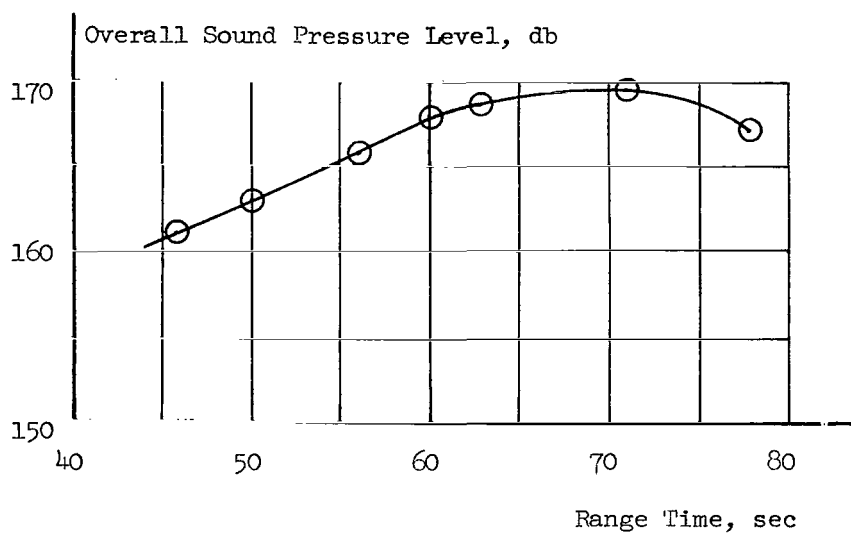FIGURE 23(c,d). POWER SPECTRAL DENSITIES OF PRESSURE FLUCTUATIONS, MEASUREMENT D159-20

54

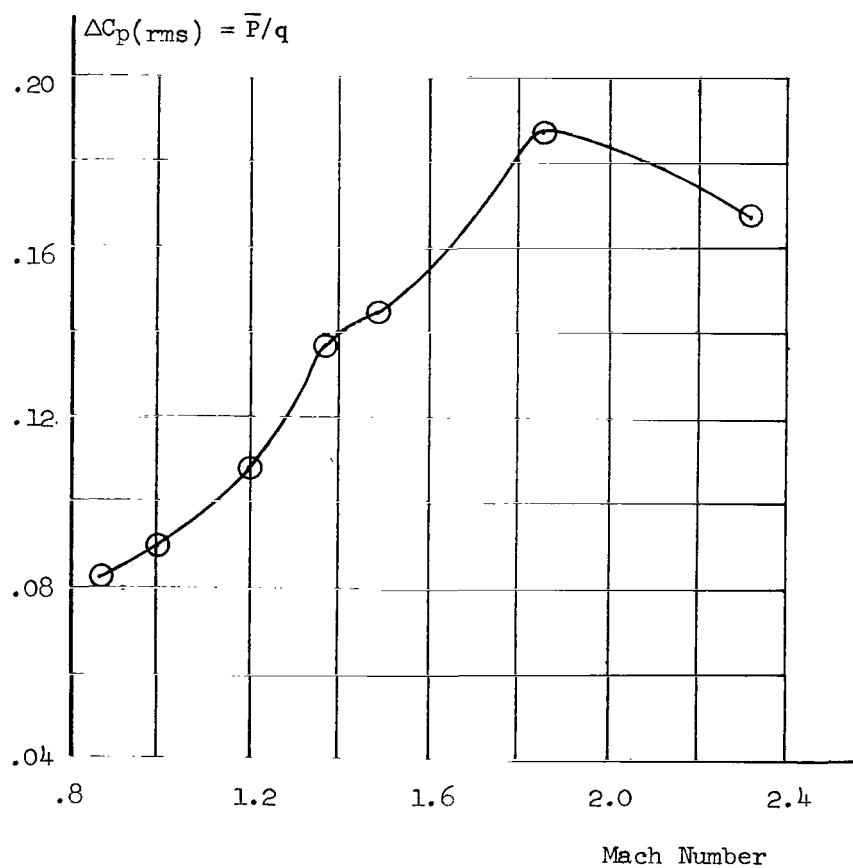FIGURE 24. OVERALL SOUND PRESSURE LEVEL VERSUS SA-4 RANGE TIME, MEASUREMENT D159-20

FIGURE 25. COEFFICIENT OF ROOT-MEAN-SQUARE PRESSURE FLUCTUATIONS ABOUT THE MEAN VERSUS MACH NUMBER, MEASUREMENT D159-20
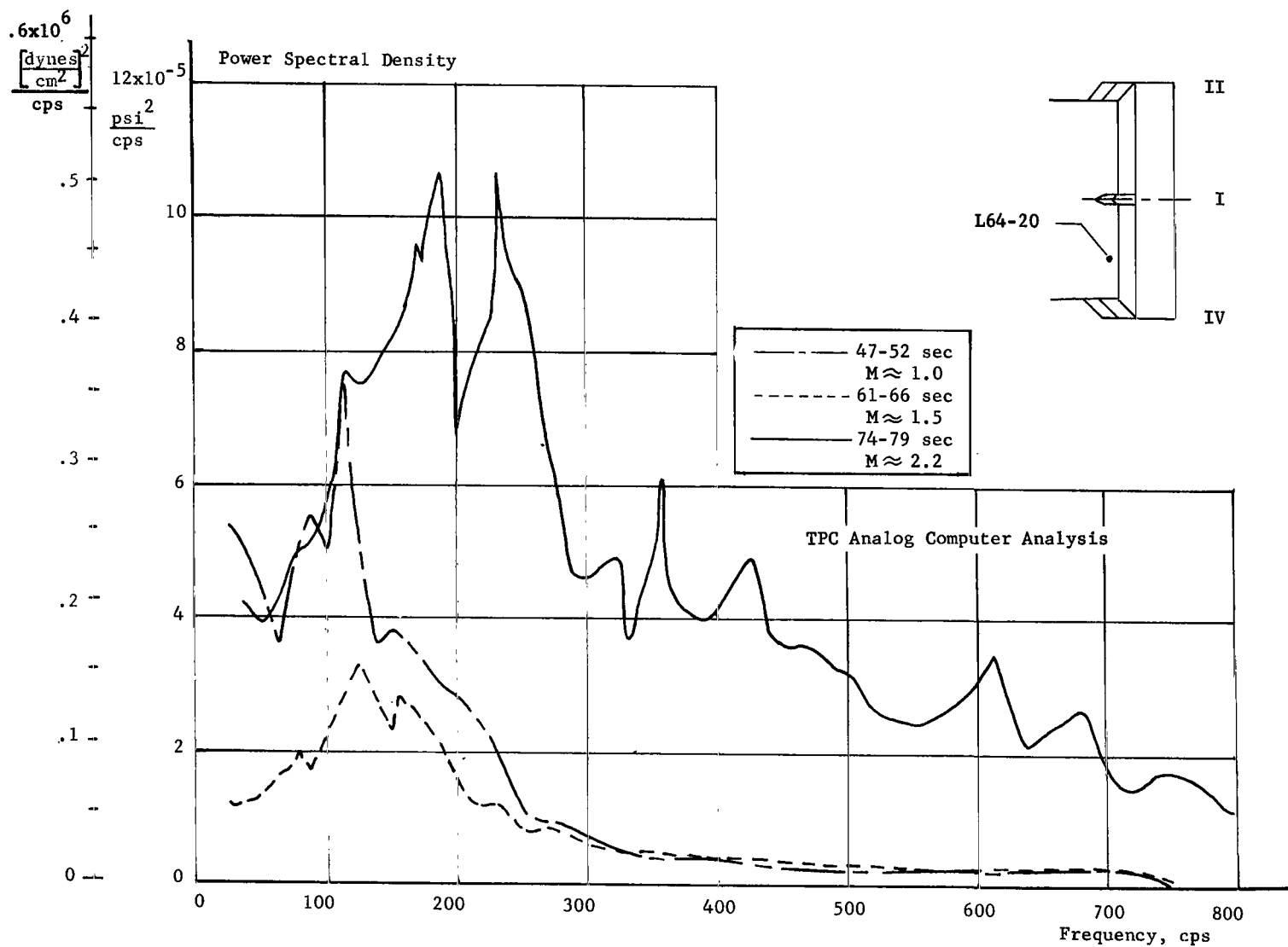
55

FIGURE 26. POWER SPECTRAL DENSITIES OF PRESSURE FLUCTUATIONS,
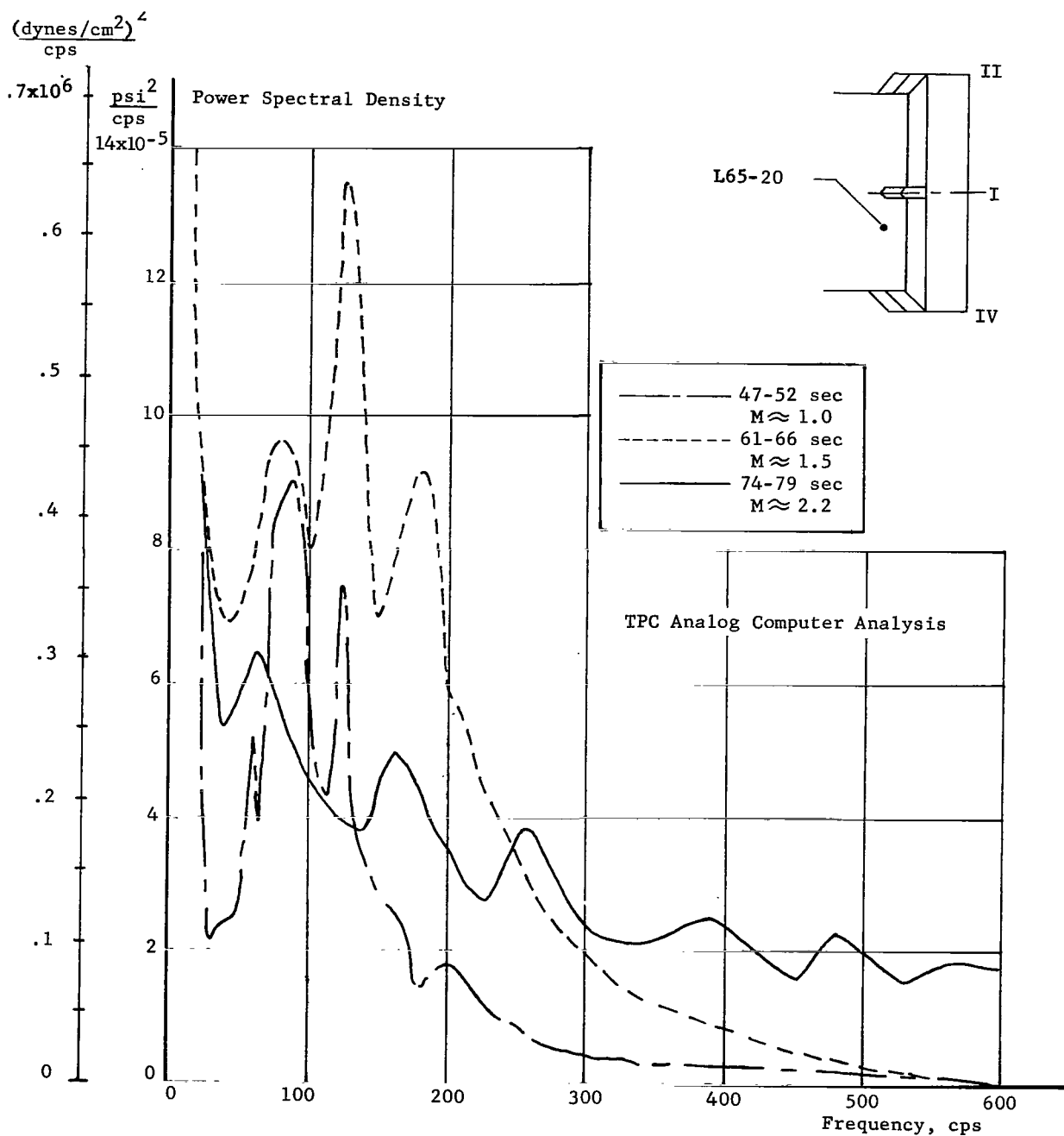MEASUREMENT L64-20

FIGURE 27. POWER SPECTRAL DENSITIES OF PRESSURE FLUCTUATIONS, MEASUREMENT L65-20